CHEMICAL AND MAGNETIC ORDER IN $Ni_2Mn_{0.8}V_{0.2}Sn$

CHEMICAL AND MAGNETIC ORDER IN THE HEUSLER ALLOY $Ni_2Mn_{0.8}V_{0.2}Sn$ BY NEUTRON DIFFRACTION

By

KENNETH E. LOCKE, B.Sc. Eng. Phys.

A Thesis

Submitted to the School of Graduate Studies

in Partial Fulfilment of the Requirements

for the Degree

Master of Science

McMaster University

June 1977

MASTER OF SCIENCE (1977)
(Physics)

McMASTER UNIVERSITY
Hamilton, Ontario

TITLE: Chemical and Magnetic Order in the Heusler Alloy $Ni_2Mn_{08}V_{0.2}Sn$ by Neutron Diffraction

AUTHOR: Kenneth E. Locke, B.Sc. Eng. Phys. (Dalhousie University)

SUPERVISOR: Professor C.V. Stager

NUMBER OF PAGES: vii, 64

ABSTRACT

Neutron diffraction techniques have been used to determine the chemical and magnetic order in a single crystal of the Heusler alloy $Ni_2Mn_{0.8}V_{0.2}Sn$. This material orders in the Heusler $L2_1$ structure and is ferromagnetic. Nuclear Bragg scattering intensity ratios have been measured at 298 K and compared with nuclear structure factor calculations based on a model of the crystal structure. This comparison is used to determine chemical disorder. Magnetic Bragg scattering intensity ratios have been measured at 117 K. These ratios, along with bulk magnetization measurements, are used to determine the spatial distribution of the magnetic moment. The crystal is found to have the $L2_1$ structure with possibly 5% or so Ni-Sn disorder. Nearly all of the magnetic moment, which is 3.19 ± .03 μ_B/mol, is found to exist on the Mn-V sites. The rest is present on the Sn atoms. The values 3.74 ± .10 μ_B/Mn atom and .21 ± .08 μ_B/Sn atom result from assuming the V atoms carry no moment.

ACKNOWLEDGEMENTS

I would like to thank my supervisor, Dr. C.V. Stager, for his companionship and instruction throughout the course of this work. I am also indebted to J. Neimanis for his technical assistance and for constructing much of the apparatus.

My thanks go to Dr. B.N. Brockhouse for many helpful hints and for use of the neutron spectrometers, to J. Couper for patiently attending to these instruments, to J. Garrett for his interest in growing the crystal and to Mrs. L. Mogensen for her typing of the manuscript.

The work was made possible through the financial support of the McMaster University Physics Department and the National Research Council of Canada.

This thesis is dedicated to my parents.

TABLE OF CONTENTS

LIST OF FIGURES

LIST OF TABLES

CHAPTER I

INTRODUCTION

Ni_2MnSn and Ni_2VSn are intermetallic compounds called Heusler alloys. The former is ferromagnetic although it is composed of elements which are normally found to be non-ferromagnetic. Nearly all of the magnetic moment exists on the Mn atoms although metallic Mn is anti-ferromagnetic. These Heusler alloys have the $L2_1$ structure. The ferro-magnetism is thought to arise from the way in which the Mn atoms are situated in this structure. A large single crystal of $Ni_2Mn_{0.8}V_{0.2}Sn$ was grown to explore the possibility of diluting the Mn sites with V. V has zero magnetic moment in Ni_2VSn and is expected to retain this property when substituted for Mn in Ni_2MnSn. An additional feature is the dependence of the magnetic properties on chemical disorder. It is the purpose of the research reported in this thesis to determine the disorder in a $Ni_2Mn_{0.8}V_{0.2}Sn$ crystal, and to establish on which sites magnetic moments exist.

The remainder of Chapter I describes Heusler alloys and presents a brief historical review. Chapter II outlines the theory behind the method of neutron diffraction. The cross-sections for nuclear and magnetic scattering are derived and topics, such as the Debye-Waller factor, absorption and extinction are discussed. A structure model for $Ni_2Mn_{0.8}V_{0.2}Sn$ is proposed and structure factors are calculated for this model. The third chapter relates how the crystal was grown, the various experiments that were done

and the apparatus involved. Chapter IV consists of the neutron diffraction data and results pertaining to the chemical and magnetic order. Chapter V contains the conclusions of this study. Improvements are proposed for future reference.

An excellent review of earlier work on Heusler alloys is found in an article by Peter J. Webster (1969). F. Heusler (1903) discovered that ferromagnetic materials could be made by alloying Cu-Mn bronze with group B elements, like Sn, Al or As.

This magnetic behaviour has interested many people and a large number of compounds have been studied.

These so-called "Heusler alloys" have many of the properties of metals, as for example, a metallic lustre and a high conductivity, but they have the structure of an ordered compound. They are therefore, classed as intermetallic compounds. The common chemical order is X_2YZ where X can be Cu, Ni, Pd, Rh or Co; Y is usually Mn and Z is a group III B or IV B element such as Al, Si, Ga, Ge or Sn.

Bradley and Rodgers (1934) were the first to determine the complete structure. They studied $(CuMn)_3Sn$ using x-rays of different wavelengths close to the absorption anomalies of Cu and Mn. The $L2_1$ structure is a four-atom basis on an FCC lattice. For Ni_2MnSn, the basis is Ni(000), Mn($\frac{1}{4}\frac{1}{4}\frac{1}{4}$), Ni($\frac{1}{2}\frac{1}{2}\frac{1}{2}$)and Sn($\frac{3}{4}\frac{3}{4}\frac{3}{4}$). A diagram is given in Fig. I-1.

Those Heusler alloys that contain Mn also have an ordered magnetic structure. Most are ferromagnetic but some have been found that are antiferromagnetic. The magnetic properties can be altered by changing the degree or type of chemical order.

Fig. I-1: Structure of Ni_2MnSn.

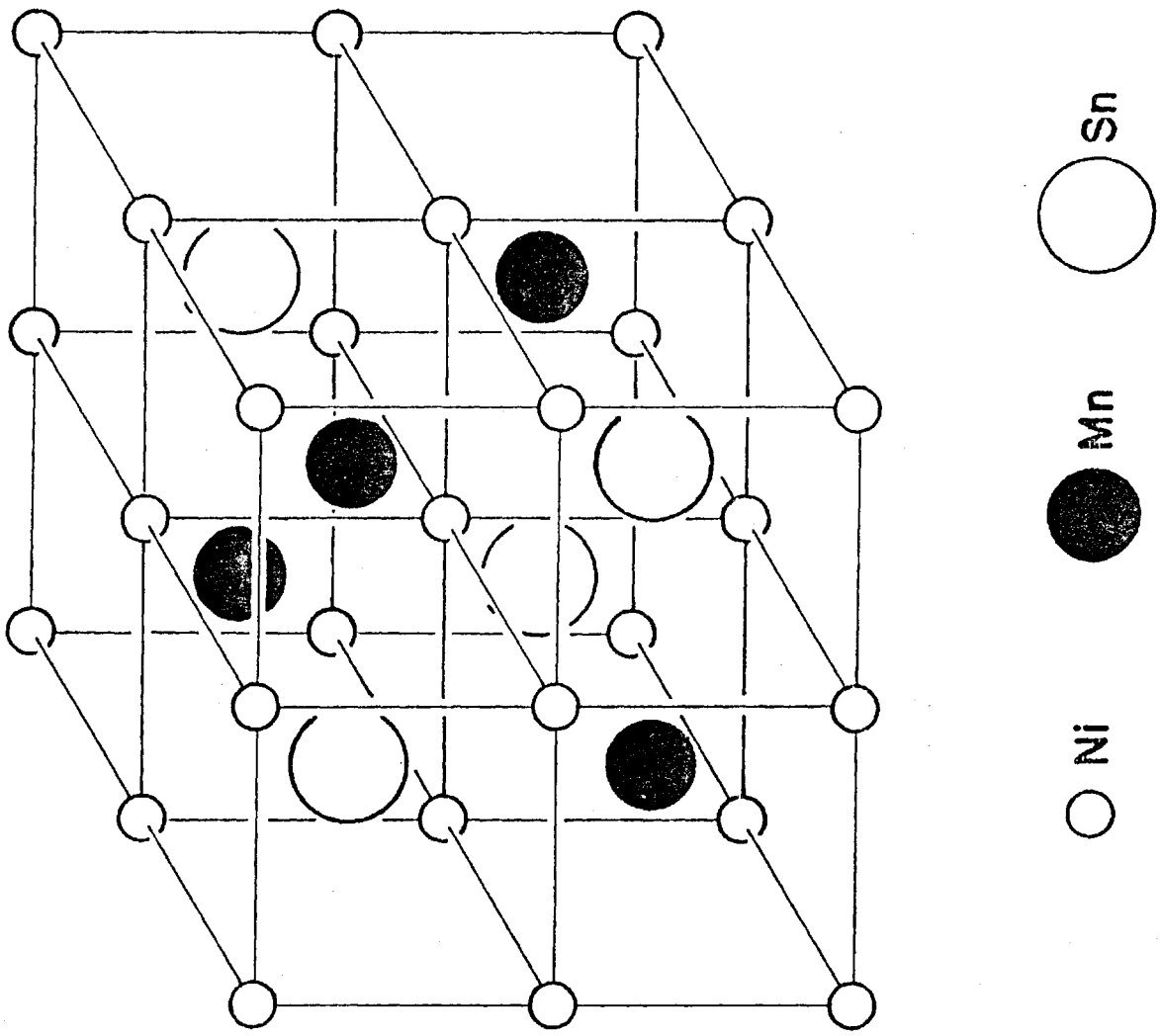
Sn
Mn
Ni

Accurate determination of magnetic and chemical structure became possible with the development of neutron diffraction. Bacon (1975) is an excellent reference for the application of neutron diffraction to these problems.

Felcher (1963) used neutron diffraction to study Cu_2MnAl using a magnetic field of 12 kOe for saturating his samples. He found that at 77 K, the magnetic moment per Mn atom was 3.7 μ_B, and that all magnetic moment was confined to the Mn site within .1 μ_B. Other studies have shown that when Mn is involved in Heusler alloys, it nearly always carries a moment of ~ 4 μ_B. A few examples given by Webster (1969) are shown in Table I-1.

There is considerable interest in the interaction mechanism between Mn atoms in Heusler alloys. Systematics with composition change and the constancy of the Mn moment argue for a localized magnetic moment, presumably arising from the Mn d-electrons. The mechanism responsible for the coupling of these moments has not been resolved. Inelastic neutron scattering experiments (Noda and Ishikawa, 1976) show that a long range oscillatory interaction exists. This suggests an s-d interaction but there are difficulties with the short range part of the interaction.

Early work on Ni_2MnSn was carried out by Castelliz (1951, 1953), Hames (1960), Johnston and Hall (1968) and Webster (1968). These people established the stability of the compound and the chemical and magnetic structure. A magnetic moment of 4.05 μ_B per atom was found to reside on the Mn atoms.

Table I-1: The magnetic moment per Mn atom in Heusler alloys.

Composition	Moment/Mn(μ_B:Bohr magnetons)
Cu_2MnAl	3.8
Cu_2MnIn	4.0
Cu_2MnSn	4.1
Ni_2MnGa	4.17
Ni_2MnIn	4.40
Ni_2MnSn	4.05
Ni_2MnSb	3.27
Co_2MnAl	4.01
Co_2MnSi	5.07
Co_2MnGa	4.05
Co_2MnGe	5.11
Co_2MnSn	5.08
Pd_2MnAl	4.4
Pd_2MnIn	4.3
Pd_2MnSn	4.23

Campbell (1975) has measured the magnetic hyperfine fields acting on the non-Mn nucleii in a large number of Heusler alloys using the Mossbauer technique. The magnitude and sign of these fields give information on the spin polarization of the conduction electrons which are responsible for the indirect magnetic interaction between the Mn atoms.

Noda and Ishikawa (1976) have studied spin waves in Pd_2MnSn and Ni_2MnSn to obtain information about the Mn-Mn interaction. Ishikawa and Tajima (1976) used polarized neutrons to accurately determine the atomic form factor of Mn^{2+} atoms in Pd_2MnSn. Magnetization measurements have been done by Campbell and Stager (1976) on the series $Ni_2Mn_xT_{1-x}Sn$ where T is Ti, V or Cr. Curie temperatures and saturation moments were recorded for polycrystalline samples. For $Ni_2Mn_{0.8}V_{0.2}Sn$, they found the Curie temperature to be 261 K and the saturation magnetization to be 3.20 μ_B/mol.

The present work was undertaken to explore the possibilities of a neutron diffraction study on the same series, $Ni_2Mn_xT_{1-x}Sn$. A single crystal of $Ni_2Mn_{0.8}V_{0.2}Sn$ was grown. It is the chemical disorder and magnetic structure of this crystal which are the subject of this thesis.

CHAPTER II

THEORY AND MODEL CALCULATIONS

The first sections of this chapter deal with the theory involved in the aspects of neutron diffraction relevant to these experiments.

This can by no means be a complete derivation of all the formulas used, but is merely a presentation of those effects that must be understood to explain the data. The topics include nuclear and magnetic scattering cross-sections, the Debye-Waller factor, absorption and extinction. The last section is a calculation of the structure factors including atomic form factors for an idealized model of a Heusler alloy. These allow the prediction of magnetic and nuclear integrated intensities and ratios.

The thermalized neutron is a unique probe into the world of atoms as well as into the more remote world of nuclei. A 1 A° neutron has .082 eV of energy, travels at a velocity of 3.95×10^3 m/s, and has a frequency of 3.95×10^{13} Hz. Its charge is zero but, rather anomalously, it has a magnetic moment of -1.91 nuclear magnetons. It is the scattering of this quantum creature by crystals to which we now turn our attention. The discussion follows closely that of Marshall and Lovesey (1971).

A. Scattering Theory

The problem of calculating the neutron scattering cross-sections

is set up as follows. A polar co-ordinate system is arranged so that a beam of incoming neutrons is travelling in the positive z-direction. It impinges on a scatterer at the origin which deflects the neutrons through the polar angle θ in some direction defined by the azimuthal angle ϕ. The incident and scattered neutrons are described as plane waves with propagation vectors $\bar{k}$ and $\bar{k}'$ respectively. The flux of incident neutrons, N, is defined as the number of particles incident on the scatterer per unit area per unit time.

The cross section for a scattering arrangement is the number of scattered particles detected per unit time divided by N. When considering scattering into a differential solid angle $d\Omega$, a differential scattering cross-section $\frac{d\sigma}{d\Omega}$ is defined such that

$$(\frac{d\sigma}{d\Omega})d\Omega = \frac{\text{(number of particles scattered into } d\Omega \text{ per unit time)}}{N}$$

Let the initial state of the system be described by the ket $|\bar{k}\sigma n\rangle$ where $\bar{k}$ refers to the neutron wave vector, σ the neutron spin, and n the initial state of the scatterer. Similarly, let $|\bar{k}'\sigma'n'\rangle$ represent the state of the neutron and scatterer after scattering. Since the cross section is related to the transition probability between $|\bar{k}\sigma n\rangle$ and $|\bar{k}'\sigma'n'\rangle$, it can be calculated, in the spirit of the Born approximation, by using Fermi's Golden Rule. The result of this calculation is the total partial differential cross-section for scattering from $\bar{k}$ to $\bar{k}'$,

$$\frac{d^2\sigma}{d\Omega dE'} = \frac{k'}{k}\left(\frac{m}{2\pi\hbar^2}\right)^2 \sum_{n,\sigma} P_n P_\sigma \sum_{n',\sigma'} |\langle \bar{k}'\sigma'n'|\hat{V}|\bar{k}\sigma n\rangle|^2 \delta(\hbar\omega + E_n - E_{n'}). \qquad (1)$$

The "totality" of the above expression is achieved by summing over all final states σ', n' that have wave vector $\bar{k}'$ and averaging over all initial states σ, n with wave vector $\bar{k}$. The coefficients P_σ and P_n are the probabilities that the incoming neutron has spin σ and that the scatterer is in the state described by n. The probabilities can be calculated by use of statistical mechanics. The partial differential $\frac{\partial}{\partial E'}$ and the delta-function build into the equation the conservation of energy condition

$$\frac{\hbar^2 k^2}{2m} + E_n = \frac{\hbar^2 k'^2}{2m} + E_{n'}$$

where

$$\frac{\hbar^2}{2m}(k^2 - k'^2) = \hbar\omega$$

E_n and $E_{n'}$ are the initial and final energies of the scatterer. $\hat{V}$ is the operator associated with the interaction potential between the neutron and scatterer.

B. Nuclear Scattering

When a neutron is scattered by a nucleus the nucleon-nucleon interaction is responsible. This is known to have a very short range, approximately 1.5×10^{-5} A°, much less than the wavelength of a thermal neutron. Therefore there can be little interference from different parts

of the nucleus and the scattering must be isotropic, S-wave scattering. It is well known that this type of scattering can be characterized by a single complex parameter b, called the scattering length. The imaginary part describes absorption processes such as radiative capture. In general, the scattering length is different for each element and isotope and is also sensitive to the spin orientation of the scatterer.

To get S-wave scattering out of our Born-approximation differential cross-section formula, we must ascribe a delta-function potential to the interaction. The Fermi pseudo-potential describes the interaction of a neutron at $\bar{r}$ with a nucleus at $\bar{R}$. It is given by

$$\hat{V}(\bar{r}) = \frac{2\pi\hbar^2}{m} b\, \delta(\bar{r} - \bar{R}). \tag{2}$$

For a rigid lattice model of a crystal with atoms at $\bar{\ell}$ this becomes:

$$\hat{V}(\bar{r}) = \frac{2\pi\hbar^2}{m} \sum_{\bar{\ell}} b_{\bar{\ell}}\, \delta(\bar{r} - \bar{\ell}).$$

$\bar{\ell}$ is a lattice vector for Bravais lattices.

For plane waves

$$\langle \bar{k}' | \hat{V} | \bar{k} \rangle = \frac{2\pi\hbar^2}{m} \sum_{\bar{\ell}} b_{\bar{\ell}} \int d\bar{r}\, \exp(-i\bar{k}'.\bar{r})\, \delta(\bar{r}-\bar{\ell})\, \exp(i\bar{k}.\bar{r})$$

$$= \frac{2\pi\hbar^2}{m} \sum_{\bar{\ell}} b_{\bar{\ell}}\, \exp(i\bar{Q}.\bar{\ell})$$

where $\bar{Q} \equiv \bar{k} - \bar{k}'$, the scattering vector. If we substitute this into

the scattering cross-section formula (Eq. 1), we obtain the result

$$\frac{d\sigma}{d\Omega} = \frac{k'}{k} \sum_{n,\sigma} P_n P_\sigma \sum_{n',\sigma'} |\langle \sigma' n' | \sum_{\bar{\ell}} b_{\bar{\ell}} \exp(i\bar{Q}.\bar{\ell}) | \sigma n \rangle|^2$$

Here n,n' refer to the distribution of isotopes and nuclear spin orientations. To obtain an idea of the form of the nuclear scattering cross-section, we make the approximation that the energy of the lattice is independent of the above distributions, therefore restricting ourselves to elastic scattering. The sum over n' and σ' can now be done by closure with the result

$$\frac{d\sigma}{d\Omega} = \sum_{n,\sigma} P_n P_\sigma \sum_{\bar{\ell}\,\bar{\ell}'} \exp\{i\bar{Q}.(\bar{\ell} - \bar{\ell}')\} \langle \sigma n | b^*_{\bar{\ell}'} b_{\bar{\ell}} | \sigma n \rangle .$$

Performing the average over the nuclear spins and isotopes and defining

$$\overline{b^*_{\bar{\ell}'} b_{\bar{\ell}}} \equiv \sum_{n} P_n \langle n | b^*_{\bar{\ell}'} b_{\bar{\ell}} | n \rangle ,$$

we obtain

$$\frac{d\sigma}{d\Omega} = \sum_{\bar{\ell}\bar{\ell}'} \exp\{i\bar{Q}.(\bar{\ell} - \bar{\ell}')\} \overline{b^*_{\bar{\ell}'} b_{\bar{\ell}}} .$$

Since $\overline{b^*_{\bar{\ell}'} b_{\bar{\ell}}} = \overline{b^*_{\bar{\ell}'}}\ \overline{b_{\bar{\ell}}} = |\bar{b}|^2$ if $\bar{\ell} \neq \bar{\ell}'$

and

$$\overline{b^{*}_{\bar{\ell}'} b_{\bar{\ell}}} = \overline{|b_{\bar{\ell}}|^2} = \overline{|b|^2} \quad \text{if } \bar{\ell} = \bar{\ell}'$$

The above can be written as

$$\overline{b^{*}_{\bar{\ell}'} b_{\bar{\ell}}} = |\bar{b}|^2 + \delta_{\bar{\ell},\bar{\ell}'}(\overline{|b|^2} - |\bar{b}|^2)$$

so that the cross section splits into two parts

$$\frac{d\sigma}{d\Omega} = \left(\frac{d\sigma}{d\Omega}\right)_{coh} + \left(\frac{d\sigma}{d\Omega}\right)_{incoh}, \tag{3a}$$

where

$$\left(\frac{d\sigma}{d\Omega}\right)_{coh} = |\bar{b}|^2 \left|\sum_{\bar{\ell}} \exp(i\bar{Q}.\bar{\ell})\right|^2, \tag{3b}$$

and

$$\left(\frac{d\sigma}{d\Omega}\right)_{incoh} = N\ \overline{|b-\bar{b}|^2}. \tag{3c}$$

These two types of scattering are very different. The coherent scattering is subject to strong interference effects and can be large if certain geometric requirements are met, or it can vanish. The incoherent scattering is isotropic.

We will concentrate on the coherent part. If it is generalized to the case where there is more than one type of atom per unit cell, then

$$\left(\frac{d\sigma}{d\Omega}\right)_{coh} = \left|\sum_{\bar{\ell}} \exp(i\bar{Q}.\bar{\ell})\right|^2 \left|\sum_{\bar{d}} \bar{b}_{\bar{d}} \exp(i\bar{Q}.\bar{d})\right|^2$$

where $\bar{d}$ is the position vector of the d^{th} atom in the unit cell. The first factor is zero unless $\bar{Q}$ is a reciprocal lattice vector $\bar{G}$ and therefore this factor is proportional to the delta function $\delta(\bar{Q}-\bar{G})$. The quantity

$$F_N(\bar{Q}) = \sum_{\bar{d}} \bar{b}_{\bar{d}} \exp(i\bar{Q}.\bar{d}), \tag{4}$$

is called the unit cell structure factor.

The coherent elastic nuclear scattering off a rigid lattice is therefore given by:

$$\left(\frac{d\sigma}{d\Omega}\right)^{el}_{coh} = \left|\sum_{\bar{\ell}} \exp(i\bar{Q}.\bar{\ell})\right|^2 |F_N(\bar{Q})|^2. \tag{5}$$

The $\bar{b}$'s in $F_N(\bar{Q})$ are determined experimentally and are tabulated (Bacon, 1975).

C. Debye-Waller Factor

The discussion so far has been restricted to a rigid lattice. When allowing for harmonic atomic oscillations it can be shown that the result for a Bravais lattice is the rigid lattice result multiplied by $\exp\{-2W(\bar{Q})\}$, the Debye-Waller factor. Since $2W(\bar{Q}) = \langle\{\bar{Q}.\hat{\bar{\mu}}\}^2\rangle$ where $\hat{\bar{\mu}}$ is the atomic displacement operator, we see that 2W is equal to the mean squared displacement of the atom perpendicular to $\bar{Q}$ multiplied by $|\bar{Q}|^2$.

Since $\langle \hat{\underline{\mu}}_{\perp}^2 \rangle = \frac{1}{3} \langle \hat{\underline{\mu}}^2 \rangle$ for cubic crystals and $|\bar{Q}| = \frac{4\pi}{\lambda} \sin\theta$ where 2θ is the scattering angle

$$W(\bar{Q}) = \frac{1}{3} \frac{8\pi^2}{\lambda^2} \sin^2\theta \langle \hat{\underline{\mu}}^2 \rangle. \tag{6}$$

When allowing for vibrations in a non-Bravais lattice, the unit cell structure factor becomes

$$F_N(\bar{Q}) = \sum_{\bar{d}} \bar{b}_{\underline{d}} \exp(i\bar{Q}.\bar{d}) \exp(- W_d(\bar{Q})). \tag{7}$$

The Debye-Waller factors tend to make the intensities fall off with increasing $\sin^2\theta$. It is important to note that because they are different for each atomic species, they do not enter $F_N(\bar{Q})$ as a simple exponential scaling factor. These factors are also temperature dependent. For temperatures above the Debye temperature, the Debye-Waller factors are linear in temperature. In the high temperature region the dependence for monatomic crystals is given by

$$W(\bar{Q}) \sim \frac{\hbar^2 |Q|^2}{2M} \frac{3k_B T}{(k_B \theta_D)^2} \{1 + \frac{1}{36}(\frac{\theta_D}{T})^2 - \frac{1}{3600}(\frac{\theta_D}{T})^4\}.$$

D. Magnetic Scattering

The magnetic interaction between the neutron and unpaired electrons is another equally-important effect. Because of the quenching of the orbital angular momentum, we restrict our attention to the spin of the unpaired electrons. There are other small effects due to the motion of

the electron which shall be neglected here so that the interaction potential is that of two dipoles $\bar{R}$ apart

$$\hat{V} = 2\gamma\mu_N\mu_B\hat{\bar{\sigma}}.\mathrm{curl}\left(\frac{\hat{\bar{S}} \times \bar{R}}{|\bar{R}|^3}\right). \tag{8}$$

The dipole moment of the neutron is $\hat{\bar{\mu}} = \gamma\mu_N\hat{\bar{\sigma}}$ and that of the electron is $\bar{\mu}_e = -2\mu_B\hat{\bar{s}}$. $\hat{\bar{\sigma}}$ and $\hat{\bar{s}}$ are the spins of the neutron and electron respectively. Substitution of this interaction into Eq. 1 for the cross-section gives

$$\frac{d^2\sigma}{d\Omega dE'} = \left(\frac{m}{2\pi\hbar^2}\right)^2(2\gamma\mu_N\mu_B)^2 \sum_{nn'\sigma\sigma'} \frac{k'}{k} P_n P_\sigma |\langle \bar{k}' n' \sigma' | \sum_i \hat{\bar{\sigma}}.\mathrm{curl}\left(\frac{\hat{\bar{S}}_i \times \hat{\bar{R}}}{|\bar{R}|^3}\right)|\bar{k} n \sigma\rangle|^2 x$$

$$x\ \delta(\hbar\omega + E_n - E_{n'}). \tag{9}$$

The sum over i is over all unpaired electrons in the atom. Using the identities

$$\frac{\bar{R}}{|\bar{R}|^3} = -\bar{\nabla}\left(\frac{1}{|\bar{R}|}\right) \; ; \quad \frac{1}{|\bar{R}|} = \frac{1}{2\pi^2}\int d\bar{q}\,\frac{1}{q^2}\exp(i\bar{q}.\bar{R})$$

part of this can be evaluated to give

$$\langle \bar{k}' | \sum_i \hat{\bar{\sigma}}.\mathrm{curl}\left(\frac{\hat{\bar{S}}_i \times \bar{R}}{|\bar{R}|^3}\right)|\bar{k}\rangle = 4\pi \sum_i \exp(i\bar{Q}.\bar{r}_i)\hat{\bar{\sigma}}.\{\tilde{Q} \times (\hat{\bar{S}}_i \times \tilde{Q})\}$$

$$\equiv 4\pi\hat{\bar{\sigma}}.\hat{\bar{T}}_\perp \tag{10}$$

where $\bar{r}_i$ is the position vector of the i^{th} electron and the symbol $\sim$ denotes a unit vector. Expressing the cross-section in terms of the tensor components of $\hat{\bar{\sigma}}.\hat{\bar{T}}_{\perp}$, allows us to write

$$\frac{d\sigma}{d\Omega} = \left(\frac{\gamma e^2}{m_e c^2}\right)^2 \frac{k'}{k} \sum_{\alpha,\beta} (\delta_{\alpha,\beta} - \tilde{Q}_\alpha \tilde{Q}_\beta) \sum_{nn'} P_n \langle n|\hat{T}_\alpha^{\dagger}|n'\rangle\langle n'|\hat{T}_\beta|n\rangle, \tag{11}$$

where we have used the fact that

$$\sum_{\sigma} p_\sigma \langle\sigma|\hat{\sigma}_\alpha \hat{\sigma}_\beta|\sigma\rangle = \delta_{\alpha,\beta}$$

for unpolarized neutrons.

For a Bravais crystal lattice, the sum in the expression for $\hat{T}$ will be over all unpaired electrons in the whole crystal. If these electrons are localized on the lattice sites, the term in the above expression becomes:

$$\langle n'|\hat{\bar{T}}|n\rangle = \sum_{\bar{\ell}} \exp(i\bar{Q}.\bar{\ell})\ f(\bar{Q})\langle n'|\hat{S}_{\bar{\ell}}|n\rangle, \tag{12}$$

where $\hat{S}_{\bar{\ell}}$ is proportional to the total spin on the atom and $f(\bar{Q})$ is the atomic form factor. It is related to the spin density $s(\bar{r})$ by:

$$f(\bar{Q}) = \int d\bar{r}\ \exp(i\bar{Q}.\bar{r}) s(\bar{r}). \tag{13}$$

The penultimate cross-section equation is

$$\frac{d\sigma}{d\Omega} = \left(\frac{\gamma_e^2}{m_e c^2}\right)^2 \frac{k'}{k} \sum_{\alpha,\beta} (\delta_{\alpha,\beta} - \tilde{Q}_\alpha \tilde{Q}_\beta) \sum_{\bar{\ell}\,\bar{\ell}'} |f(Q)|^2 \exp\{i\bar{Q}.(\bar{\ell}' - \bar{\ell})\} x$$

$$X \sum_{n,n'} P_n \langle n|\hat{S}_{\bar{\ell}}^{\alpha}|n'\rangle\langle n'|\hat{S}_{\bar{\ell}'}^{\beta}|n\rangle. \tag{14}$$

Finally, if the material is ferromagnetic and all spins are aligned in a certain direction $\tilde{\eta}$, the spin on each site can be expressed in terms of the average spin, giving

$$\sum_{n,n'} P_n \langle n|\hat{S}_{\bar{\ell}'}^{\alpha}|n'\rangle\langle n'|\hat{S}_{\bar{\ell}'}^{\beta}|n\rangle = \delta_{\alpha,z}\delta_{\beta,z}\langle \hat{S}^z\rangle^2. \tag{15}$$

Thus, the cross-section for elastic-coherent magnetic scattering is

$$\left(\frac{d\sigma}{d\Omega}\right)_{coh}^{el} = \left|\sum_{\bar{\ell}} \exp(i\bar{Q}.\bar{\ell})\right|^2 \{1 - (\tilde{Q}.\tilde{\eta})^2\}_{av} \{\left(\frac{\gamma_e^2}{m_e c^2}\right)\langle \hat{S}\rangle |f(\bar{Q})| \exp(-W(\bar{Q}))\}^2. \tag{16}$$

E. Combined Scattering

The total cross-section for elastic coherent Bragg scattering off a ferromagnetic material with all spins aligned in a direction $\tilde{\eta}$, allowing for interference between those scattered by nuclear and magnetic interactions, is:

$$\frac{d\sigma}{d\Omega} = \left|\sum_{\bar{\ell}} \exp(i\bar{Q}.\bar{\ell})\right|^2 [|F_N(\bar{Q})|^2 + 2\,\tilde{\eta}.\bar{P}_\perp R_e F_N(\bar{Q}) F_m^*(\bar{Q}) + q^2 |F_M(\bar{Q})|^2], \tag{17a}$$

where

$$F_N(\bar{Q}) = \sum_{\bar{d}} \overline{b_{\bar{d}}} \exp(i\bar{Q}.\bar{d}) \exp(-W_d(\bar{Q})), \tag{17b}$$

$$F_M(\bar{Q}) = \sum_{\bar{d}} P_{\bar{d}} \exp(i\bar{Q}.\bar{d}) \exp(-W_d(\bar{Q})), \tag{17b}$$

$$P_{\bar{d}} \equiv \left(\frac{\gamma_e^2}{m_e c^2}\right) \langle \hat{S}_d \rangle |f_d(\bar{Q})| \exp(-W_d(\bar{Q})), \tag{17d}$$

$$q^2 \equiv \{1 - (\tilde{Q}.\tilde{n})^2\}_{av}, \tag{17c}$$

and $\bar{P}_{\perp}$ is the polarization of the incoming neutrons. For unpolarized neutrons, the interference term averages to zero and the intensities of the two types of scattering are additive. $P_{\bar{d}}$ is a magnetic quantity analogous to the nuclear scattering length. The expression allows for different atomic species in the unit cell. It is written for magnetic spin angular momentum scattering but orbital angular momentum can be accounted for by adding a factor $\frac{g_{\bar{d}}}{2}$ in $P_{\bar{d}}$ where $g_{\bar{d}}$ is the Landé splitting factor of the atom at $\bar{d}$ in the unit cell.

It was mentioned above that $|\sum_{\bar{\ell}} \exp(i\bar{Q}.\bar{\ell})|^2$ was a delta function for $\bar{Q} = \bar{G}$, a reciprocal lattice vector. Written out in full, the expression is

$$\hbar\bar{k} - \hbar\bar{k}' = \hbar\bar{G}$$

which is a conservation of momentum condition if $\hbar\bar{G}$ is considered the

momentum of a crystal excitation. This is also Bragg's scattering law since $|\bar{Q}| = \frac{4\pi\sin\theta}{\lambda}$ and $|\bar{G}_{hk\ell}| = \frac{2\pi}{d_{hk\ell}}$ implying that $\lambda = 2d_{hk\ell}\sin\theta$. Experimentally, the Bragg scattering is not a delta-function for it is blurred by the mozaic spread of the crystals, the degree of collimation of the spectrometer and the wavelength spread in the neutron beam. The correct intensity ratios can still be obtained by integrating over a "rocking curve" since the integrated intensity is proportional to

$$Q_{2\theta} = \frac{\lambda 3|F_N(\bar{G})|^2}{v_o{}^2 \sin 2\theta} \quad (cm^{-1}), \tag{18}$$

where $\frac{1}{\sin 2\theta}$ is the Lorentz factor.

To determine magnetic structure, we must be able to measure the magnetic scattering intensities to fit them to a model. Often the magnetic peaks occur at the same scattering angles as the nuclear peaks rendering some means of distinguishing them necessary. It is possible to use the fact that the magnetic scattering lengths have an additional form factor dependence which causes the magnetic intensities to decrease more rapidly with increasing $\frac{\sin\theta}{\lambda}$. However, the most convenient method of separation, apart from using polarized neutrons, is to adjust the factor q^2. $\bar{q}$ is known as the magnetic interaction vector. If a magnet is used to point all the spins in a ferromagnet in a direction $\tilde{n}$ such that $\tilde{Q}.\tilde{n} = 1$ (i.e., magnetize the sample along the scattering vector) then q^2 will be zero and only the nuclear intensity will be present.

However, if no magnetic field is applied to the sample, it will break up into randomly oriented domains and q^2 will average out to 2/3. The nuclear intensity plus 2/3 the magnetic intensity shows up.

Subtracting the intensities obtained in these two cases gives 2/3 the magnetic scattering intensity, measurable as required.

F. Absorption and Extinction

There are two other effects that tend to decrease the scattered neutron intensities, namely absorption and secondary extinction. Absorption decreases the intensity by the factor

$$A(\mu) = \frac{1}{V}\int_{\text{crystal}} \exp[-\mu(T_1 + T_2)]dV, \tag{19}$$

where T_1 and T_2 are the path lengths in and out of the crystal.

μ is the absorption coefficient. Secondary extinction is when mozaic blocks in the front part of the crystal diffract away neutrons so that the incident intensity on more remote areas of the crystal is diminished. The end effect is similar to absorption and it was shown by Darwin (1922) that extinction can be accounted for by modifying the absorption coefficient μ to an effective coefficient μ' where $\mu' = \mu + gQ_{2\theta}$. g is a constant which depends on the mozaic spread of the crystal and $Q_{2\theta}$ is defined above (Eq. 18). Since the true absorption coefficient μ for $Ni_2Mn_{0.8}V_{0.2}Sn$ is only .225 cm^{-1}, it can be neglected. Extinction, however, shows up quite markedly for low angle, high intensity peaks causing observed intensities to depend on crystal shape. A detailed analysis is possible for certain crystal shapes as shown by Hamilton (1957) and Zacharison (1967).

G. Disorder Model Predictions for $Ni_2Mn_{0.8}V_{0.2}Sn$

Ni_2MnSn is a Heusler alloy of stoichiometric composition X_2YZ. It has the $L2_1$ crystal structure. The allowed reflections and relative intensities are determined by calculating its structure factors. Structure factors are calculated by using Eq. (4)

$$F_N(\bar{G}) = \sum_{\bar{d}} \bar{b}_{\bar{d}} \exp(i\bar{G}.\bar{d})$$

$$= \sum_{\bar{d}} \bar{b}_{\bar{d}} \exp\{2\pi i(\frac{hx_d}{a} + \frac{ky_d}{a} + \frac{\ell z_d}{a})\}, \qquad (20)$$

where h, k, ℓ, are the Miller indices of the reflection planes corresponding to the reciprocal lattice vector $\bar{G}$, and $\frac{x_d}{a}$, $\frac{y_d}{a}$, $\frac{z_d}{a}$ are the co-ordinates of the atom at $\bar{d}$ in the unit cell. The Debye-Waller factors have been omitted here. For Ni_2MnSn, there are three groups of allowed hkℓ-reflections. These are described below.

h,k,ℓ	all odd	eg. (111)
h,k,ℓ	all even and $\frac{h+k+\ell}{2}$ odd	(200)
h,k,ℓ	all even and $\frac{h+k+\ell}{2}$ even	(220)

The corresponding structure factors are:

$$F_N(111) = 4|b_Y - b_Z|$$
$$F_N(200) = 4|b_Y + b_Z - 2b_X| \qquad (21)$$
$$F_N(220) = 4|b_Y + b_Z + 2b_X|$$

As a prelude to a possible study of the series $Ni_2Mn_xT_{1-x}Sn$ where T is Ti, V, Cr or Fe, a crystal of $Ni_2Mn_{0.8}V_{0.2}Sn$ was grown. In this crystal, the Y site can be occupied by either a Mn or a V atom since Ni_2MnSn and Ni_2VSn are ismorphous. Furthermore, disorder can occur between the X, Y and Z sites, strongly affecting the observed intensities. To obtain agreement between measured and calculated structure factors, one must propose a reasonable model of the disorder. The various disorder parameters can be adjusted to fit predicted to measured intensities. The formulas below and calculations, which are reported in Table II-1, assume that there is no chemical disorder and that all moments are located on the Mn sites.

The nuclear structure factors are given by:

$$\begin{aligned} F_N(111) &= 4|.8b_{Mn} + .2b_V - b_{Sn}| \\ F_N(200) &= 4|.8b_{Mn} + .2b_V + b_{Sn} - 2b_{Ni}| \\ F_N(220) &= 4|.8b_{Mn} + .2b_V + b_{Sn} + 2b_{Ni}|. \end{aligned} \tag{22}$$

The scattering lengths used are given in Table II.1.

To determine the magnetic scattering structure factors predicted by this model, one must first find the different magnetic scattering lengths for Mn when involved in the (111), (220) and (220) reflections. The magnetic scattering lengths are given by

$$P = \left(\frac{\gamma_e^2}{m_e c^2}\right)\langle S\rangle\, f(\bar{Q}), \tag{23}$$

where γ = - 1.913148 and for Mn , <S> = 2. The dependence on the reflection planes is through the atomic form factor $f(\bar{Q})$. This factor has been determined experimentally for Mn in Ni_2MnSn by Y. Ishikawa and K. Tajima (1976) as a function of

$$\frac{\sin\theta}{\lambda} = \frac{(h^2 + k^2 + \ell^2)^{1/2}}{2a}.$$

The atomic form factors in Table II-1 were obtained from their graph. The magnetic structure factors are given by

$$F_M(hk\ell) = 4|p(hk\ell)|, \tag{24}$$

for the model where all of the magnetic scattering originates from the Mn sites.

The calculations for this model are presented in Table II-1. The experimentally observed intensities should be proportional to

$$\frac{|F|^2}{\sin 2\theta}$$

if the model is correct. A convenient parameter for comparison is the ratio of the magnetic intensities to the nuclear intensities.

Table II-1: Predictions based on ordered model with all moments on Mn site

Nuclear Scattering Lengths (cm)		Magnetic Scattering Lengths		
$b_{Ni} = 1.03 \times 10^{-12}$		(hkℓ)	f(form factor)	P_{Mn} (cm)
$b_{Mn} = -.36 \times 10^{-12}$		111	.794 ± .005	$-(8.56 \pm .06) \times 10^{-13}$
$b_{V} = -.051 \times 10^{-12}$		200	.741 ± .005	$-(7.99 \pm .06) \times 10^{-13}$
$b_{Sn} = .61 \times 10^{-12}$		220	.557 ± .005	$-(6.01 \pm .06) \times 10^{-13}$
(hkℓ)	$\lvert F_N \rvert^2 (cm^2)$	$\lvert F_m \rvert^2 (cm^2)$		$\lvert F_m^2 / \lvert F_N \rvert^2$
111	$(1.320 \pm .026) \times 10^{-23}$	$(7.51 \pm .09) \times 10^{-24}$		.569 ± .018
200	$(4.89 \pm .11) \times 10^{-23}$	$(6.54 \pm .09) \times 10^{-24}$		.134 ± .005
220	$(9.00 \pm .15) \times 10^{-23}$	$(3.69 \pm .08) \times 10^{-24}$		.041 ± .002

CHAPTER III

SAMPLE PREPARATION AND EXPERIMENTAL APPARATUS

A. Crystal Growth

The neutron scattering experiments were performed on three crystals of $Ni_2Mn_{0.8}V_{0.2}Sn$. They were all cut from one large single crystal and differed only in shape and volume. The large single crystal was grown at McMaster University using the Czochralski method.

The Czochralski method of growing single crystals is to freeze the top of a melt onto a rod and slowly draw the solid out of the melt. More of the liquid will freeze on at the solid-liquid interface and by carefully controlling the speed of pulling and temperature of the melt, one can obtain a single crystal of the desired shape and size. A major advantage to this method is the ease of control due to the fact that the crystal can be seen.

Enough of each element to make 150 g of $Ni_2Mn_{0.8}V_{0.2}Sn$ was weighed out to the nearest 0.0001 g. The material was put into an Al_2O_3 crucible which fits into a graphite suceptor which in turn fits inside the coils of an r-f induction furnace. (See Fig. III-1). At McMaster, the furnace used was an Arthur D. Little MP furnace; the r-f generator was a 30 kW model made by Thermonic; and the device for controlling temperature was a Leeds and Northrup AZAR Power Control Unit. The graphite susceptor couples to the r-f field and heats up

Fig. III-1: The Czochralski method of growing single crystals.

(a) at the start

(b) later

(a)

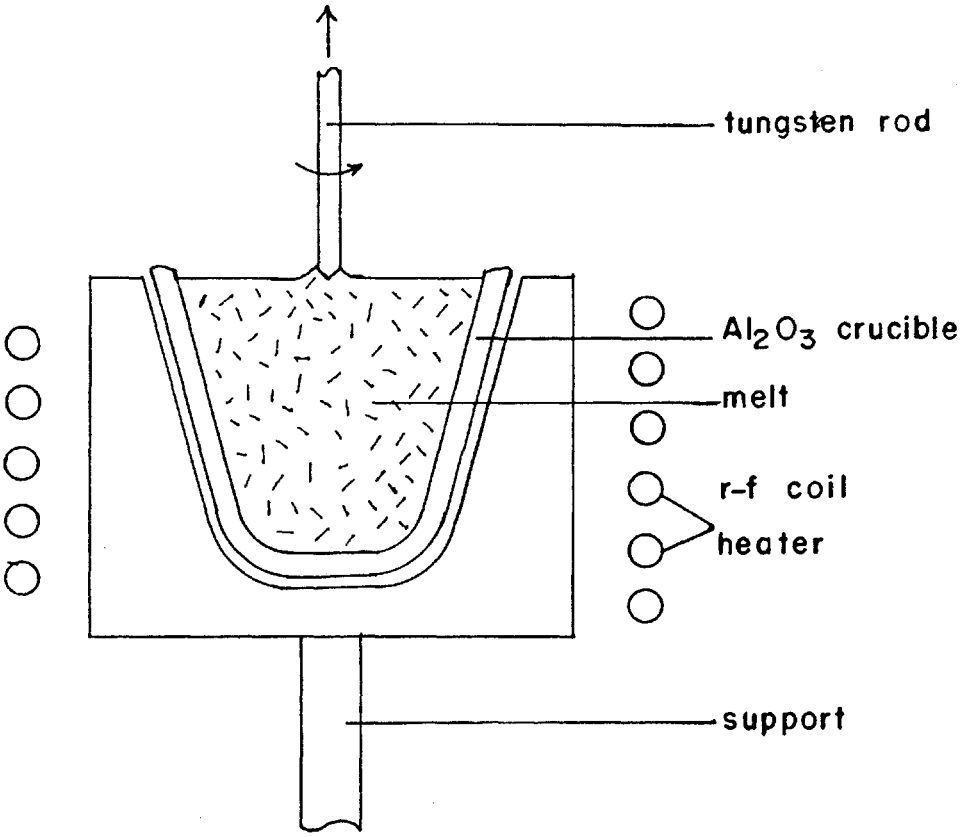
tungsten rod
Al_2O_3 crucible
melt
r-f coil
heater
support

(b)

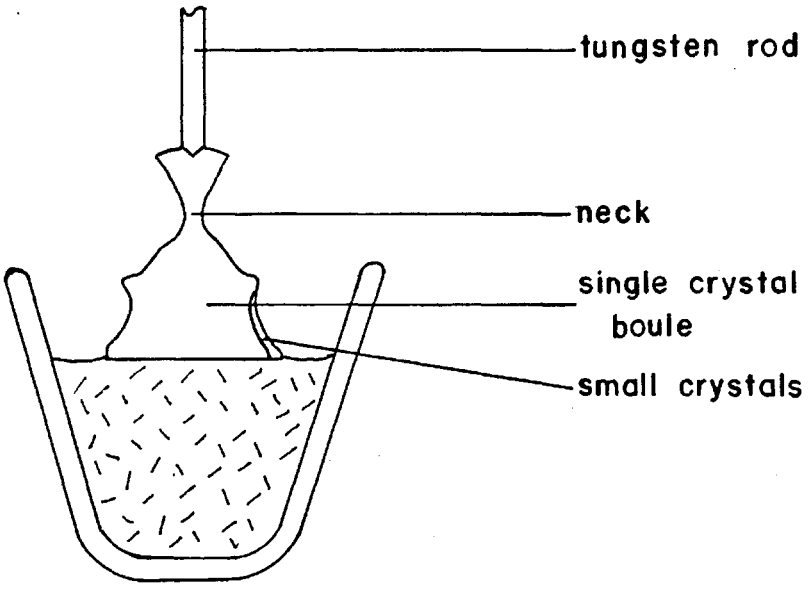
tungsten rod
neck
single crystal
boule
small crystals

causing the material in the crucible to melt.

Once the material was melted, a tungsten rod was lowered into the melt and the temperature was dropped until small crystals formed on the rod. This solid portion was then "necked down" by slightly raising the temperature until it was observed, by the way it reflected light, that only one crystal touched the melt. This single crystal was enlarged and grown to a suitable size. To ensure radial symmetry and mixing of the melt, the rod was rotated at 10 rpm.

The major problem encountered in this growth was the presence of small aggregates of extraneous material floating in the melt. When they got caught on the boule new crystallites were formed. The contamination was thought to be oxides of Mn. Fortunately, the little crystals remained small and close to the edge of the boule. This could be seen after the bottom of the crystal was polished and etched. About 95% of the boule was a single crystal.

This Heusler alloy is easily cut by spark erosion and the various crystals used were cut from the boule as shown in Fig. III-2. They are referred to as crystal #1, #2 and #3.

B. Composition Analysis

After the crystal was grown, its composition was checked and its bulk magnetic moment measured to compare with polycrystalline samples previously studied (Campbell and Stager, 1976). The results of these tests have direct bearing on the chemical order and magnetic moment distribution determinations.

Fig. III-2: The cutting of samples from the main boule.

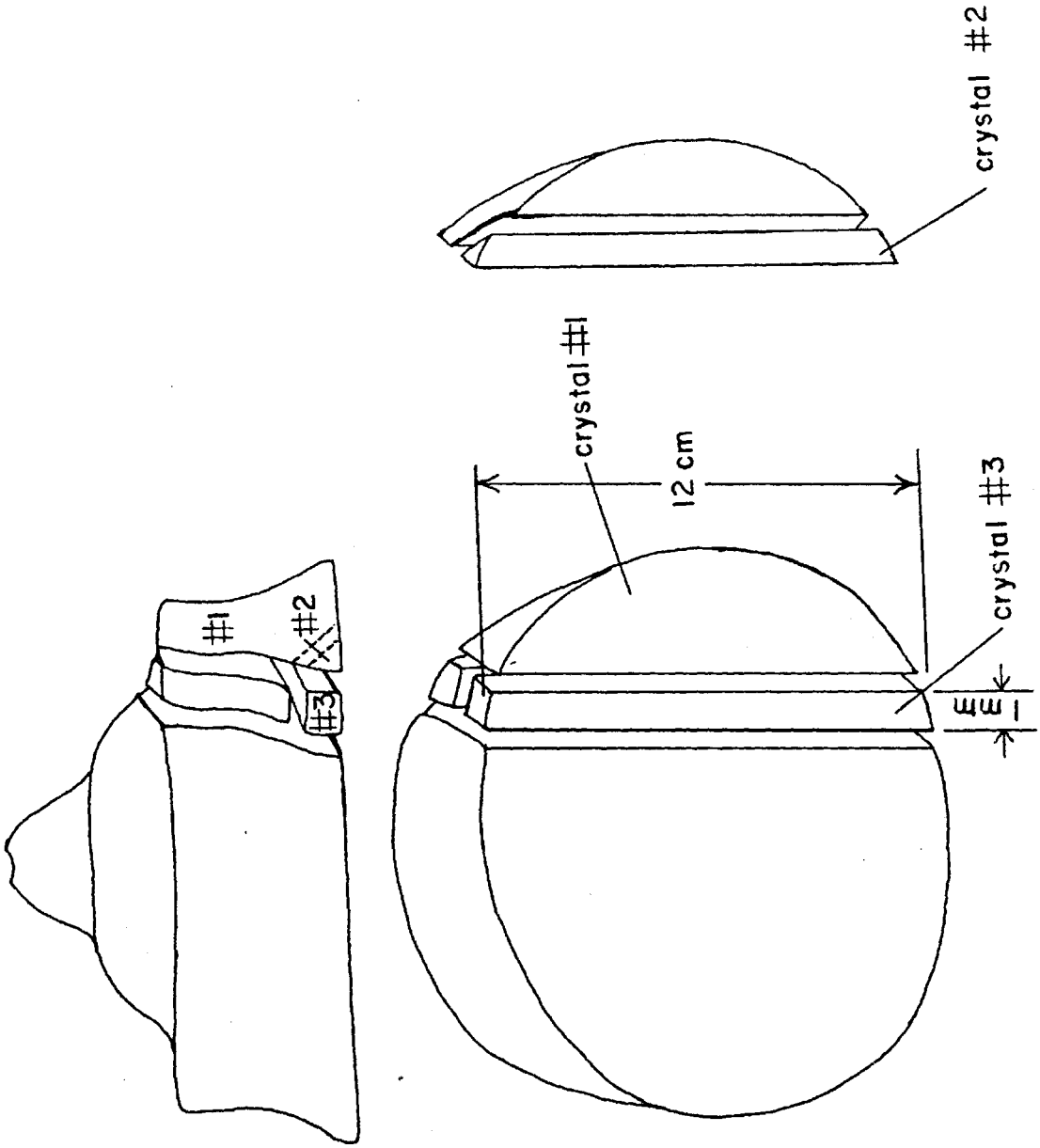
crystal #2
crystal #1
12 cm
crystal #3
#1
#2
#3

It was possible that the grown crystal was of different composition than the material weighed into the crucible because Mn is such a volatile material. Also, the crystal might not have grown with the same composition as the melt, due to effects such as the Y site being preferentially occupied by Mn over V.

Some of the elemental ratios were measured by M. Patterson and W.V. Prestwich who are developing (at McMaster University) the technique of "neutron capture gamma-ray analysis" (NCGA).

NCGA is a method of analytical spectroscopy. The sample is exposed to the high flux of thermal neutrons next to the core of a reactor while the resulting radiation is detected and the intensities measured.

When a neutron is captured by a nuclide, it exists in the capture state for a time of order 10^{-14} s before the product nuclide de-exites by emmission of gamma-rays. These are called "prompt" gamma rays because they are produced almost immediately after capture. They are detectable if the sample is accessible while being bombarded. NCGA measures these prompt gamma rays. The product nuclide may then decay by emitting a β^- particle. This second product nuclide can also emit gamma rays but these appear later than the initial capture of the neutron at times determined by the half-life for β-decay. Measurement of this delayed radiation is the traditional method of "neutron activation analysis" (NAA).

NCGA is ideal for bulk analysis because the neutrons and resulting gamma rays are highly penetrating (the gamma ray energies are the order of MeV). The energy of the emitted photons depends on the energy

levels of the product nuclide so each nuclide will display a unique γ-ray spectrum. The energy levels will be different for each isotope but since natural abundances are usually constant, the amount of element present may be deduced.

Part of the $Ni_2Mn_{0.8}V_{0.2}Sn$ boule was powdered and analyzed along with some other Heusler alloy samples. Elemental standards were examined to determine expected spectra. The ratio of $Mn:Ni_2$ obtained was .79 ± .02 and of $V:Ni_2$ was .20 ± .01. These results are in good agreement with the starting composition of the melt.

C. Bulk Magnetization Measurements

Bulk magnetic moment measurements were made with a vibrating sample magnetometer. This apparatus vibrates a sample between two pick-up coils in an arrangement where a large magnetic field can be applied. A signal proportional to the amplitude of vibration, the frequency of vibration and the magnetic moment of the sample is induced in the coils. This is compared to a reference signal proportional to the amplitude of vibration. Conventional electronics is then employed to produce a dc voltage proportional to the magnetic moment. Standard cryogenic techniques are employed for low temperature magnetization studies.

A plot of magnetization vrs temperature for $Ni_2Mn_{0.8}V_{0.2}Sn$ in a field of $\sim$ 100 Oe is given in Fig. III-3. The Curie temperature is seen to be 262 ± 3 K. The sample should be well magnetized below 150 K The magnetization vrs field at 4.2 K is shown in Fig. III-4. Extrapolation of the curve to zero magnetic field gives a magnetic moment of

Fig. III-3: Magnetization vrs temperature for $Ni_2Mn_{0.8}V_{0.2}Sn$

Tc = 262 ± 3 K

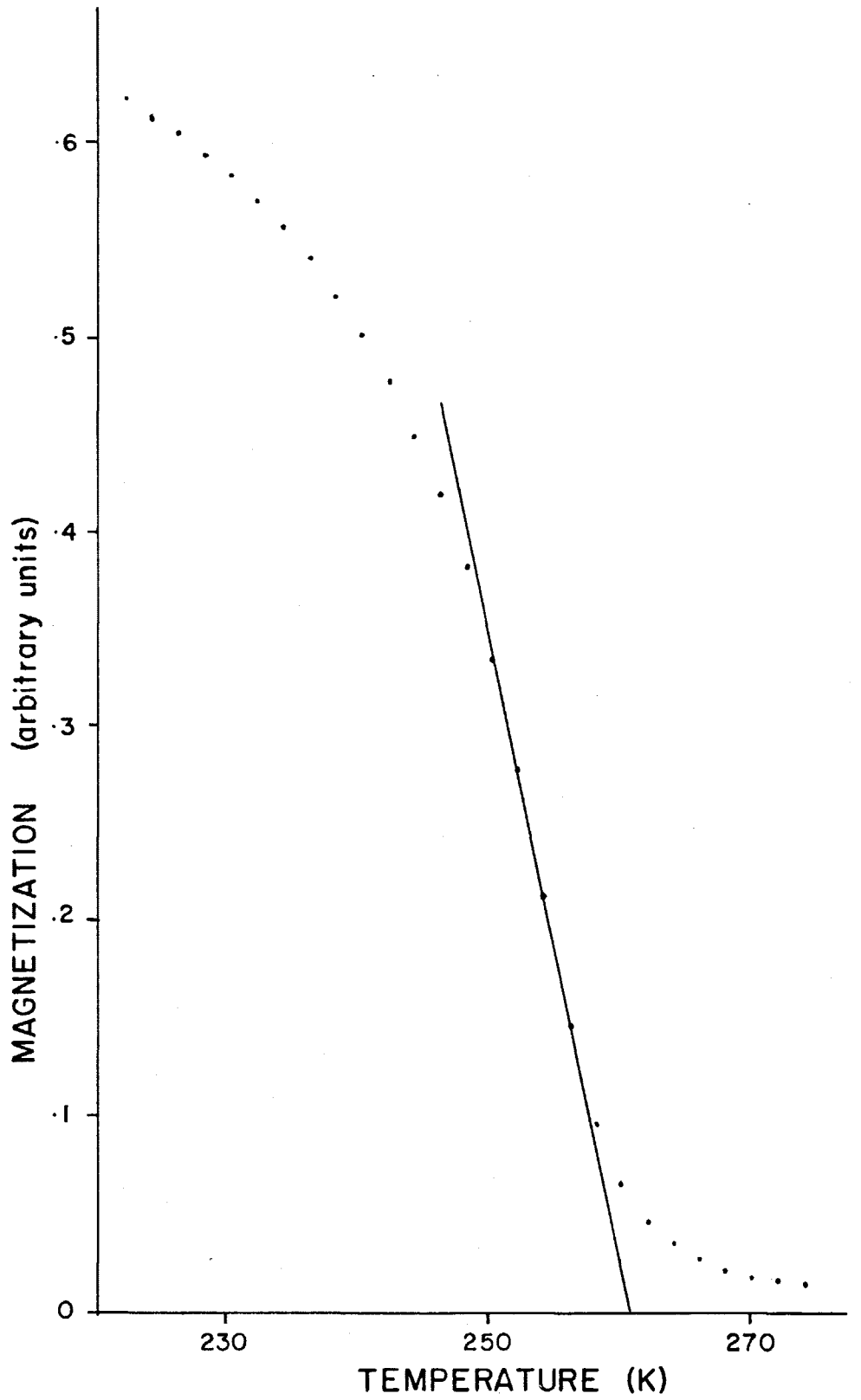
MAGNETIZATION (arbitrary units)
0
.1
.2
.3
.4
.5
.6
230
250
270
TEMPERATURE (K)

Fig. III-4: Magnetization vrs magnetic field for $Ni_2Mn_{0.8}V_{0.2}Sn$.
T = 4.2 K

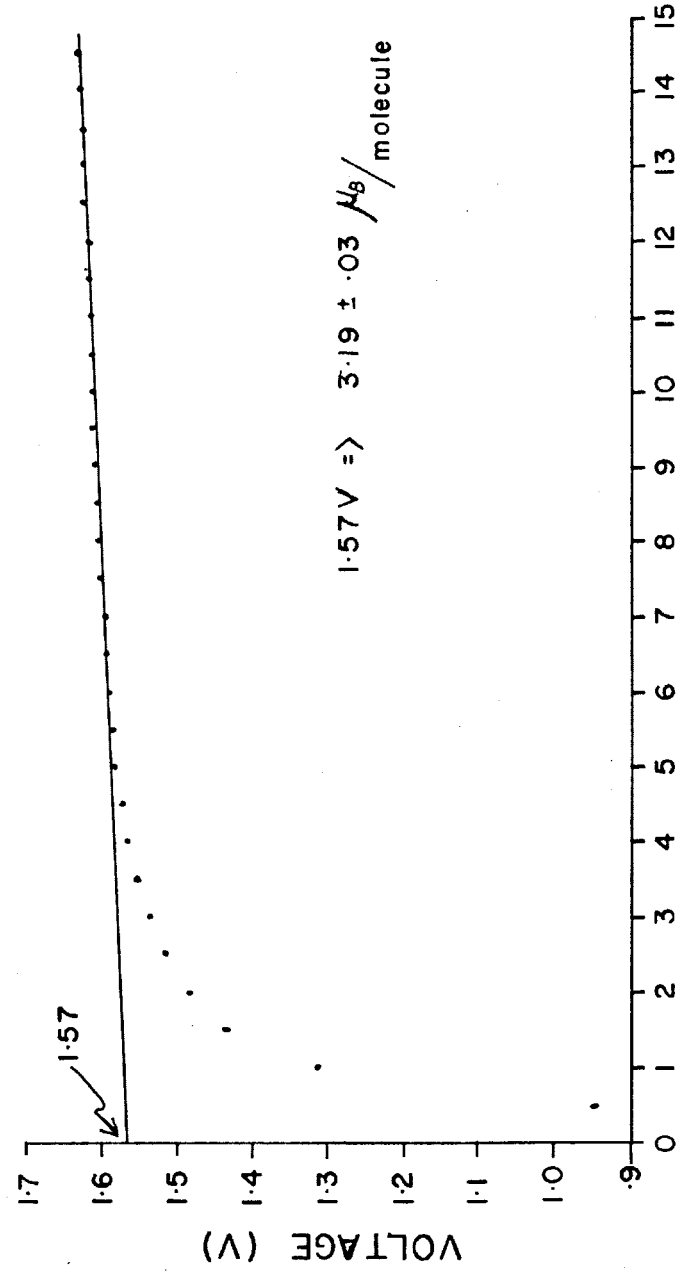
VOLTAGE (V)
1·7
1·6
1·5
1·4
1·3
1·2
1·1
1·0
·9
1·57
0 1 2 3 4 5 6 7 8 9 10 11 12 13 14 15
B (kG)
1·57 V ⇒ 3·19 ± ·03 μB/molecule

3.19 ± .03 μ_B per molecule in good agreement with data on polycrystalline samples (Campbell and Stager, 1976). This value is consistent with the expectation that each Mn atom has a moment of 4 μ_B and the alloy contains 0.8 Mn atoms per molecule.

D. The Neutron Spectrometer

The major experiments done in this study made use of three neutron spectrometers; the double-axis and triple-axis spectrometers at the McMaster University Reactor (Rowe, 1966) and the McMaster E-2 triple-axis spectrometer in the N.R.U. building at the Atomic Energy of Canada Laboratories in Chalk River, Ontario (Hallman, 1969). All of these machines are quite extensively documented in the references and only the modes used and changes related to these experiments need be discussed here.

The basic concept of a thermal neutron spectrometer is to project a collimated beam of monoenergetic neutrons onto a single crystal or powder specimen and detect those that scatter off at specific angles. The primary source of thermalized neutrons is a nuclear reactor. To aid in the following discussion, please refer to the schematic drawing of the Chalk River spectrometer in Fig. III-5. The shaping of the neutron beam begins with a hole in the reactor wall (A) into which may be inserted a rough collimator. Out of this hole comes a beam about 3" in diameter with an angular divergence of 1.5°. The energy spread of the neutrons is a Maxwellian distribution.

This beam impinges upon a large single-crystal monochromator (B), the

Fig. III-5: Schematic of Chalk River triple-axis spectrometer.

A hole in reactor wall

B single crystal (double) monochromator

C Monochromatic beam

D beam incident on specimen

E beam gate

F fission chamber monitor

G Soller slit collimators

H sample angling apparatus

I counter angling apparatus

J helium counters

K parafin and cadmium shielding barrel

L analysing crystal

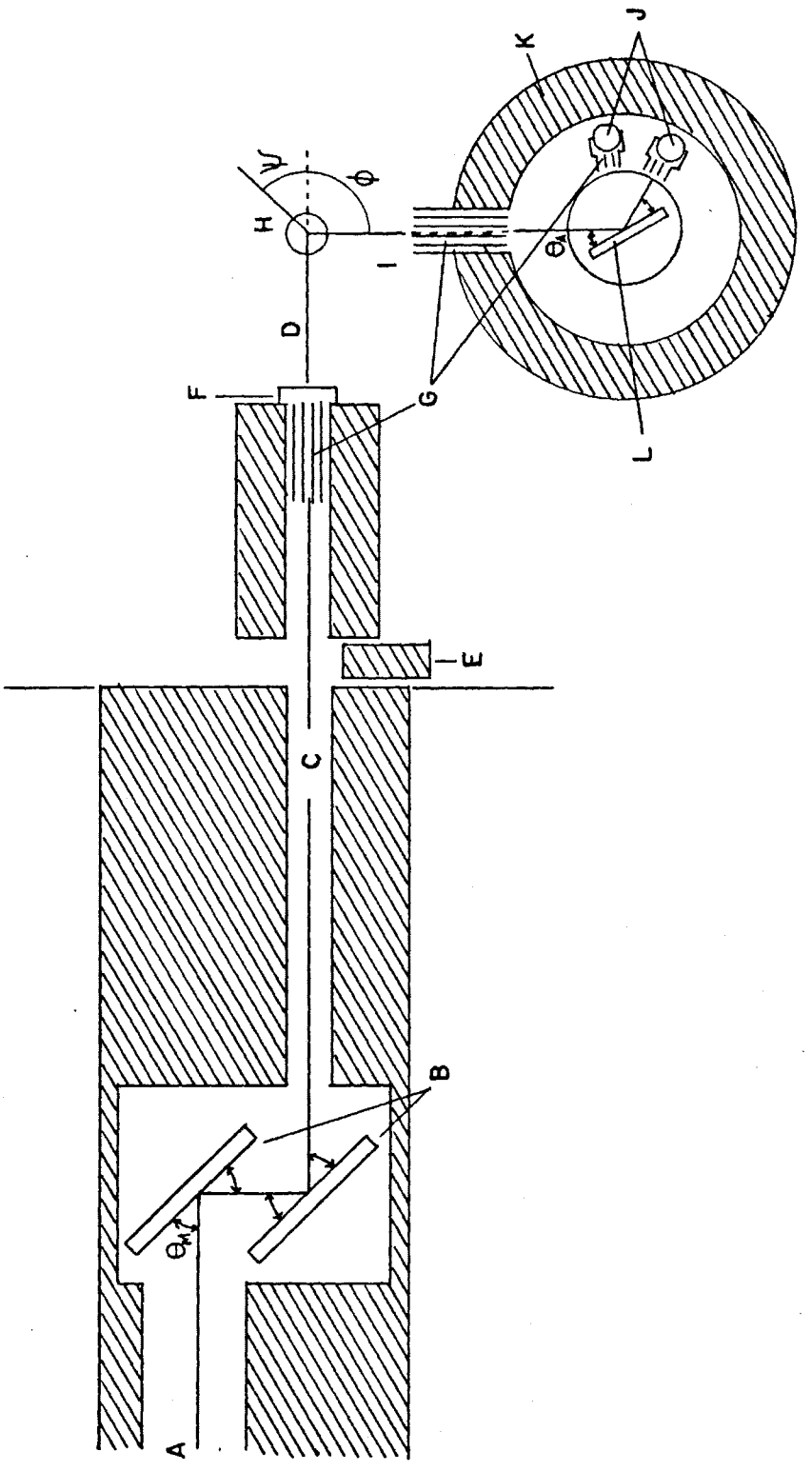
A
B
C
D
E
F
G
H
I
J
K
L
ψ
φ

angle and position of which can be adjusted to give a wide range of wavelengths, λ_0. A list of the monochromators and wavelengths used is given below.

McMaster	double-axis	(220) aluminum	1.041 A°
	triple-axis	(331) copper	1.001 A°

and

Chalk River	triple-axis	(220) copper	1.15 A°

Although the beam is essentially monochromatic at (C), the mozaic spread of the crystal causes there to be a distribution in wavelengths, centered about λ_0, and a directional divergence. The choice of crystal and final collimation ultimately determine the resolution of the spectrometer. The beam incident on the specimen (D) is typically about 1.5" square.

The striking feature of a neutron spectrometer is its size. Its movable parts are cumbersome and heavy, in contrast to similar x-ray machines, to allow for furnaces and low temperature dewars, magnets and bulky parafin shielding. The parts described below are standard to all neutron spectrometers. There is a beam gate (E) made of boron in aluminum, a low efficiency fission chamber (F) for monitoring the incoming flux (typical efficiency, 8×10^{-5}), machined holders for placement of Soller slit collimators (G), and sample and counter angling apparatus (H & I). The specimen table angle is locally referred to as ψ and the angle that the counter makes with the straight

through beam is called ϕ. Both angles are indexed in .1° steps. The counter (J) is a small cylinder of high pressure He^3 gas with a detection area of about 3 in ^{2}. It is approximately 70% efficient and is located a meter away from the specimen inside a barrel of shielding (K).

In addition, the triple-axis spectrometers have an analysing crystal (L) inside this barrel to select scattered neutron energies in inelastic scattering experiments. However, this was removed and the counter set in the straight through position.

The two-axis spectrometer was used to examine crystal #1 at room temperature. Preliminary neutron experiments on the whole boule made it evident that extinction was a sizable effect so crystal #1 was prepared. This was simply attached to a goniometer with plasticene and mounted on the specimen table. The crystal orientation was approximately set by x-rays and then more accurately adjusted on the neutron spectrometer. By this method, the (011) direction was aligned with the specimen table rotation axis within 1°. ψ was scanned for a number of Bragg peaks while ϕ was set at the 2θ angle for each reflection. The relevant data obtained are the integrated intensities.

Analysis of this data suggested further experiments on a still smaller crystal. Thus some of the peaks were scanned again in the same way using crystal #2 on the triple-axis spectrometer.

The final set of data was collected at Chalk River. The separation of magnetic scattering from nuclear scattering required that the Huesler alloy be well below its Curie temperature and in a saturating magnetic field. This was achieved by the special nitrogen dewar and

magnet arrangement described below.

On the sample table was placed an aluminum plate to support the magnet and on top of this was built a dewar table to support the dewar. The dewar was free to rotate on the dewar table and its angle of rotation could be measured.

Referring to Fig. III-6, the dewar was a small two chamber nitrogen dewar constructed out of thin-walled stainless steel. Its holding time was about 6 hours. It was discovered that due to the large coherent scattering cross-section of nitrogen (13.4 barns) it was best to fill the inner chamber with an exchange gas (helium) instead of liquid nitrogen as previously planned. This kept the sample at 117 K, well below its Curie temperature (262 K).

The sample was mounted on the end of a mechanical assembly which enabled adjustment of the crystal orientation at liquid nitrogen temperature. This assembly fitted inside the inner chamber and is detailed in Fig. III-7. To inhibit movement when the magnetic field was applied, the narrow crystal #3 was glued inside a hole drilled in a carefully shaped narrow aluminum rod. The glue was G.E. 7031 varnish. A copper-constantan thermocouple was placed next to the crystal holder.

The magnet was an aircooled electromagnet with a 0-30A constant current power supply. The frame had to be enlarged and the pole pieces tapered to allow greater access by the neutron beam (max ϕ angle $\simeq 45°$) while maintaining large magnetic field. With the poles set at 3/32" from the sides of the dewar, giving a gap of 7/8", the magnetic field obtained at 30 A was $\sim$ 8 KOe. The magnet orientation was adjusted so

Fig. III-6: Nitrogen dewar for positioning sample in magnetic field.

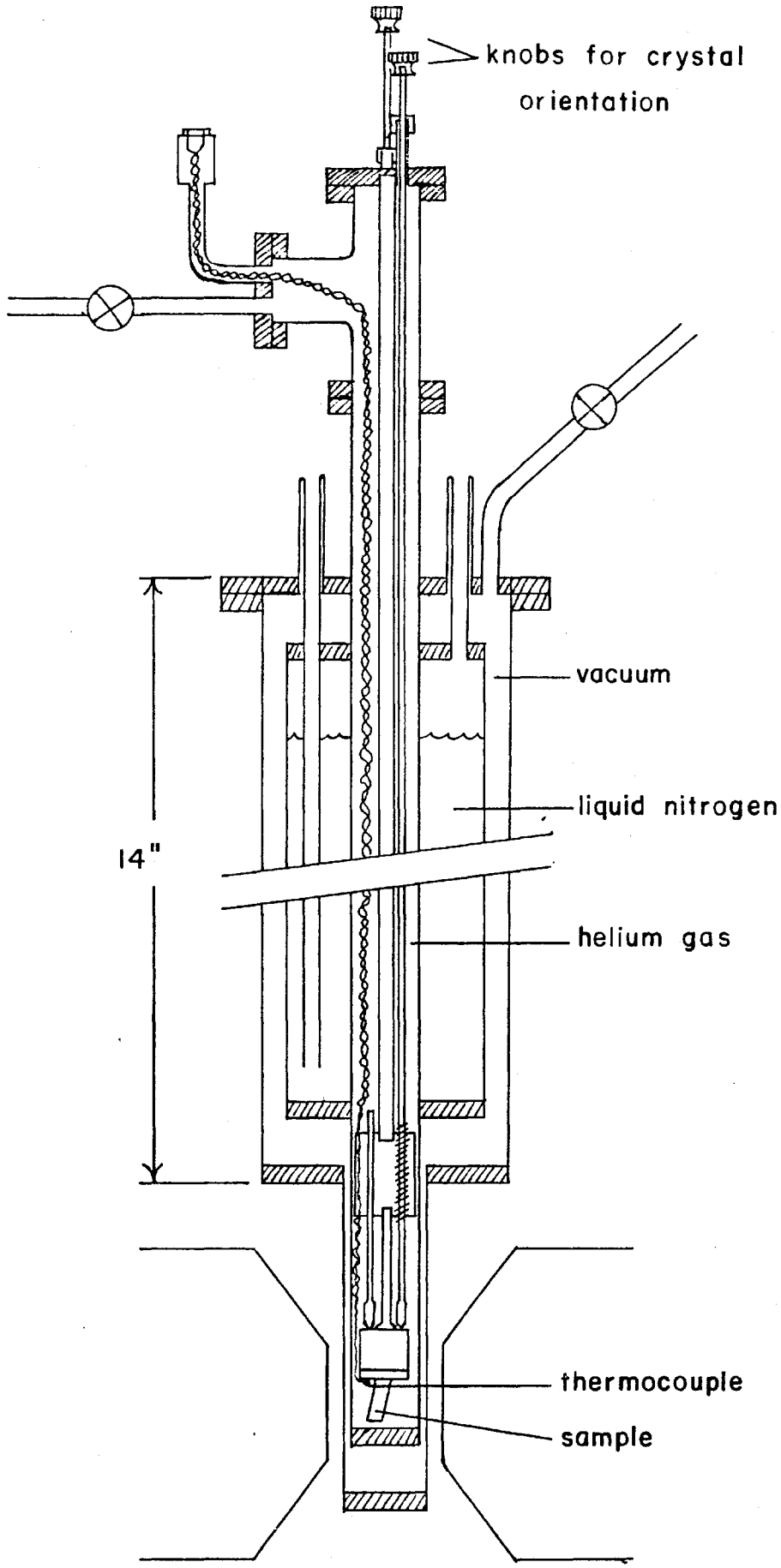
knobs for crystal orientation
vacuum
liquid nitrogen
14"
helium gas
thermocouple
sample

Fig. III-7: Low temperature Goniometer.

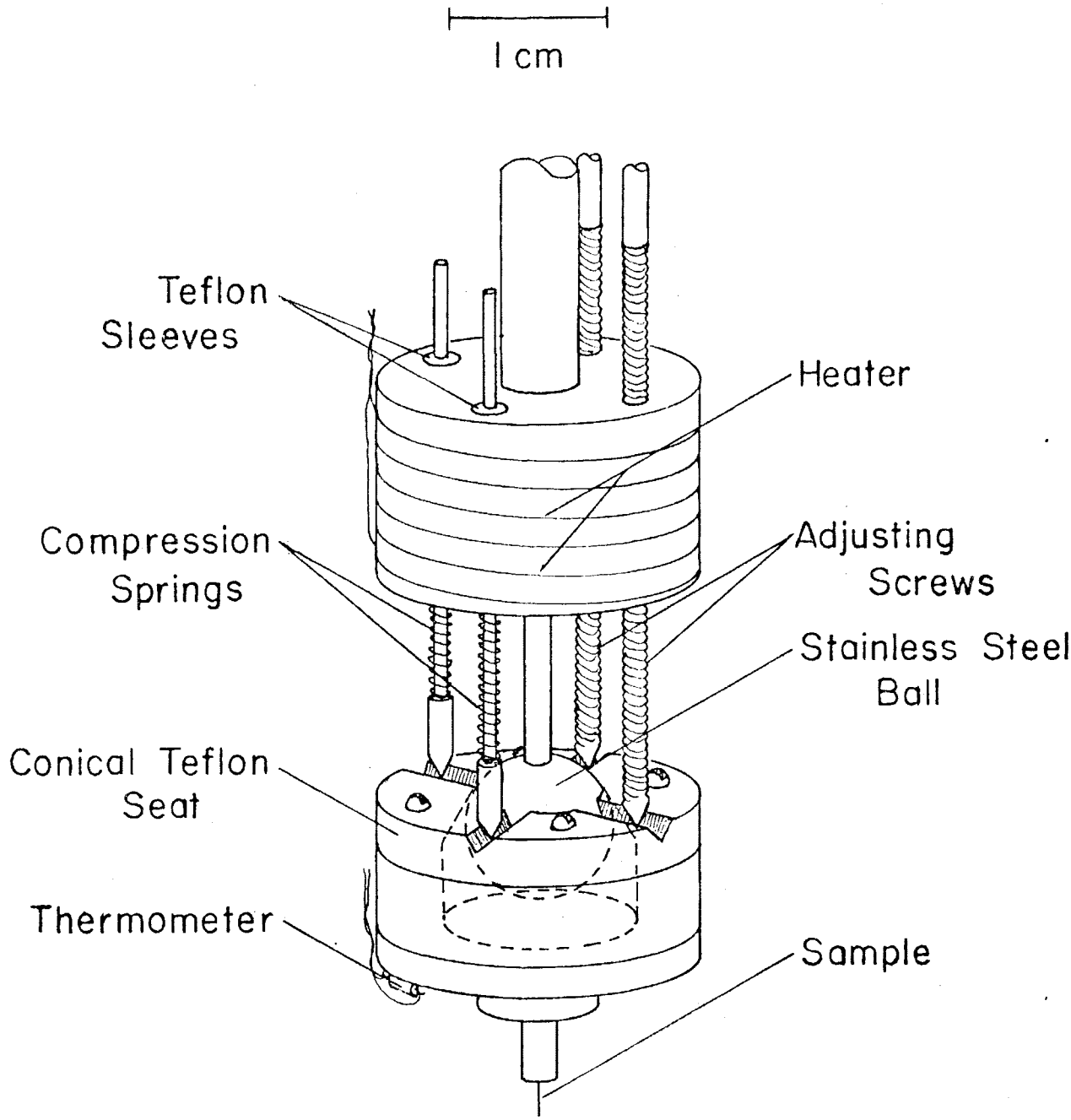
1 cm
Teflon Sleeves
Heater
Compression Springs
Adjusting Screws
Stainless Steel Ball
Conical Teflon Seat
Thermometer
Sample

that the magnetic field would be parallel to the scattering vector for each reflection.

CHAPTER IV

EXPERIMENTAL DATA AND DISCUSSION

This chapter contains a presentation and discussion of the neutron scattering data and results pertaining to $Ni_2Mn_{0.8}V_{0.2}Sn$. The information sought is the chemical and magnetic order. With each sample, the Bragg peaks were scanned in .1° steps. At each step, the scattered neutrons were counted for a certain number of monitor counts. If one plots counts vrs angle in a histogram, the integrated area under the peak can be approximated by simply adding together all the counts taken at each step and subtracting the background. The total angle swept over must be sufficiently wide to get an accurate measurement of the background. Background counts arise from incoherent scattering in the sample and dewar and from stray neutrons.

Errors occur due to the statistical nature of counting experiments. These can be reduced at the expense of long counting times. Efficiency requires proper choice of monitor efficiency and counting times. If N_i is the number of counts obtained in the interval i, the statistical error in N_i is $\sqrt{N_i}$ and the error in N_i due to the statistical error in the monitor setting M is $\frac{N_i}{\sqrt{M}}$. The total error in N_i is therefore

$$\Delta N_i = \left[\frac{N_i^2}{M} + N_i\right]^{1/2}$$

and the error in the total number of counts under the peak, N is

$$\Delta N = \left[\frac{\sum_i N_i^2}{M} + N\right]^{1/2}$$

where the sum is over the intervals which make up the peak. The error in the background was usually negligible compared to ΔN. The data for crystal #1 is shown in Table IV-1. It was taken on the double-axis spectrometer at McMaster using neutrons of wavelength λ = 1.041 A° and a monitor setting of 5000 counts. The sample was at room temperature. In Table IV-1(a) are given the scattering angles 2θ, the integrated intensities and the statistical errors. For a particular set of planes, the 2θ-angle setting changes with the neutron wavelength.

The intensities for each set of symmetry related reflections are averaged and corrected for the Lorentz factor to get $I_o \equiv I \sin 2\theta$. They are presented in Table IV-1(b) along with $(\sin\theta/\lambda)^2$ and in $\ln I_o$. The table is divided into three sections corresponding to the three structure factor groups.

When I_o is plotted against $(\sin\theta/\lambda)^2$, each group appears to lie on an exponential curve apart from the two anomalous points (220) and (400). Therefore, $\ln I_o$ vrs $(\sin\theta/\lambda)^2$ is plotted in Fig. IV-1. The points fall on three straight lines of roughly the same slope.

In Fig. IV-1, the points (220) and (400) are thought to be low because of extinction. The extinction effect causes scattered neutron intensities to become dependent on the size and shape of the sample. The intensities can be much lower for some crystal orientations than for others. This is discussed in a paper by Hamilton (1957). The two anomalies can be explained by the irregular shape of crystal #1.

Table IV-1: Bragg peak intensities for crystal #1 at room temperature.

(a) monitor 5000 λ = 1.041 A° (McMaster double axis)

(hkℓ)	2θ	I	ΔI	(hkℓ)	2θ	I	ΔI
$1\bar{1}1$	17.13°	6449	110	$51\bar{1}$	53.10°	2007	90
$11\bar{1}$		5920	110	$\bar{5}1\bar{1}$		1928	80
$\bar{1}1\bar{1}$		6381	100	$\bar{5}11$		1943	80
$\bar{1}11$		5881	100	$33\bar{3}$	53.10	2032	80
$\underline{2}00$	19.81	18138	170	$3\bar{3}\bar{3}$		1806	80
$\bar{2}00$		17742	170	$\bar{3}3\bar{3}$		1823	80
$0\bar{2}\underline{2}$	28.16	15549	160	$\bar{3}\bar{3}3$		1883	80
$02\bar{2}$		16934	160	$0\bar{4}\underline{4}$	58.25	9033	130
$3\bar{1}1$	33.15	3283	90	$04\bar{4}$		9396	130
$31\bar{1}$		3279	90	$\underline{6}00$	62.15	4596	100
$\bar{3}1\bar{1}$		3171	70	$\bar{6}00$		4638	100
$\bar{3}11$		3364	80	$2\bar{4}\underline{4}$	62.15	4388	100
$2\bar{2}\underline{2}$	34.68	10084	130	$2\underline{4}\bar{4}$		4590	100
$\underline{2}2\bar{2}$		8911	120	$\bar{2}4\bar{4}$		4654	100
$\bar{2}2\bar{2}$		9784	130	$\bar{2}\underline{4}4$		4380	100
$\bar{2}\bar{2}2$		9053	120	$5\bar{3}\underline{3}$	68.68	1373	70
$\underline{4}00$	40.25	8127	120	$5\underline{3}\bar{3}$		1234	70
$\bar{4}00$		8207	120	$\bar{5}3\bar{3}$		1437	70
$1\bar{3}\underline{3}$	44.05	2145	80	$\bar{5}\bar{3}3$		1341	70
$\underline{1}3\bar{3}$		2269	80	$6\bar{2}\underline{2}$	69.60	3903	90
$\bar{1}3\bar{3}$		2305	80	$6\underline{2}\bar{2}$		3689	90
$\bar{1}\bar{3}3$		2114	80	$\bar{6}2\bar{2}$		4127	90
$4\bar{2}\underline{2}$	49.86	11655	140	$\bar{6}\bar{2}2$		3535	90
$42\bar{2}$		10803	130	$4\bar{4}\underline{4}$	73.17	6531	110
$\bar{4}2\bar{2}$		11825	140	$44\bar{4}$		6563	110
$\bar{4}\bar{2}2$		11074	130	$\bar{4}4\bar{4}$		6672	110
$5\bar{1}1$	53.10	1943	80	$\bar{4}\bar{4}4$		6211	110

Table IV-1: Bragg peak intensities for crystal #1 at room temperature.

(b) Averaged over symmetry related reflections and corrected for Lorentz factor.

(hkℓ)	$(\sin\theta/\lambda)^2$	$I_o = I\sin 2\theta$	$\ln I_o$
111	.02048	7255 ± 60	8.8894
311	.07513	7162 ± 90	8.8765
331	.1297	6141 ± 110	8.7227
511	.1844	6323 ± 130	8.7519
333	.1844	6033 ± 130	8.7050
533	.2937	5016 ± 130	8.5204
200	.02732	24320 ± 170	10.0991
222	.08197	21526 ± 140	9.9770
600	.2459	16329 ± 240	9.7007
442	.2459	15926 ± 170	9.6757
622	.3005	14297 ± 160	9.5678
220	.05466	30660 ± 210	10.3307
400	.1093	21108 ± 220	9.9574
422	.1639	34674 ± 210	10.4537
440	.2186	31342 ± 300	10.3527
444	.3279	24864 ± 210	10.1212

Fig. IV-1: $\ln I_o$ vrs $(\sin\theta/\lambda)^2$ for nuclear peak intensities I_o.

T = 298 K
Crystal #1 = ●
Crystal #2 = X
Crystal #3 = +

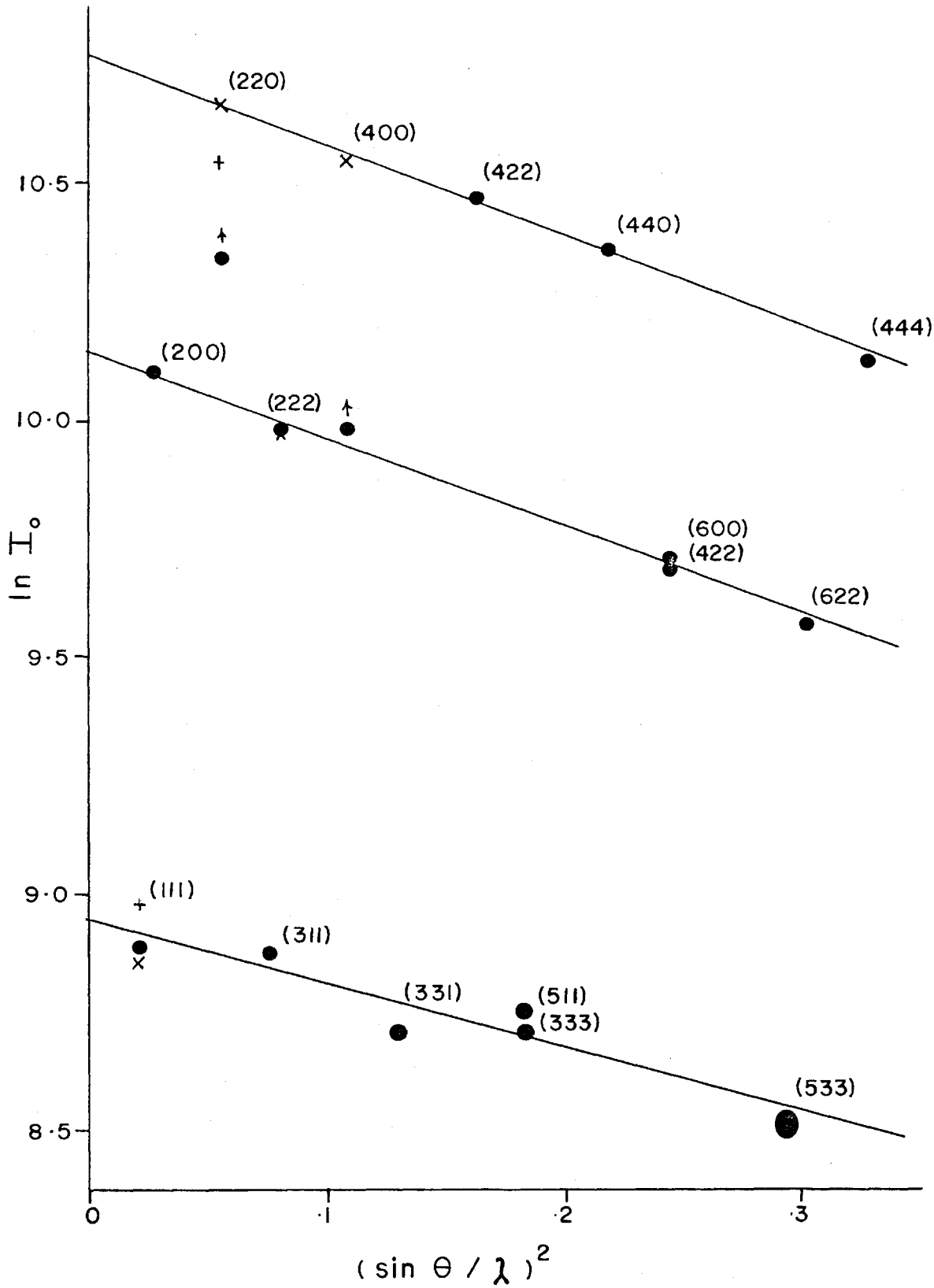
(220)
(400)
(422)
(440)
(444)
(200)
(222)
(600)
(422)
(622)
(111)
(311)
(331)
(511)
(333)
(533)
10·5
10·0
9·5
9·0
8·5
ln H°
0
·1
·2
·3
(sin θ / λ)²

To remedy this, crystal #2 was cut reducing the volume by a factor of ten and giving a more symmetrical shape. The data for this crystal is given in Table IV-2. It was taken on the triple axis spectrometer at McMaster at room temperature using neutrons of wavelength λ = 1.001 A°. Since the (200) group of the crystal #1 data gave the best straight line, the crystal #2 data was normalized to the (200) reflection (i.e., the intensities were adjusted so that the (200) intensities from each crystal were the same). This data is also plotted in Fig. IV-1. It is observed that the use of the smaller crystal reduced the large extinction effect so that the (220) and (400) points now fall on their line.

The lines were least squares fitted to the points and the results are presented in Table IV-3.

The fact that within a group of reflections, the intensities fall off exponentially with $(\sin\theta/\lambda)^2$ is consistent with the theory of the Debye-Waller factor, under certain assumptions. Since $W_d(\bar{Q})$ is related to the mean squared vibration amplitude of the atom at $\bar{d}$ in the unit cell, it depends both on the particular atom involved and the nature of the crystal site. For non-Bravais lattices, these are not simple scaling factors and the fall off in intensities is not expected to be simply exponential. The structure factor should look like:

$$F(200) = (0.8b_{Mn}e^{-W_{Mn}} + 0.2b_{V}e^{-W_{V}} + b_{Sn}e^{-W_{Sn}} - 2b_{Ni}e^{-W_{Ni}}).$$

Within the accuracy of this experiment, however, the lines in Fig. IV-1 appear to be straight. This suggests that the Debye-Waller factors for

Table IV-2: Bragg peak intensities for crystal #2 at room temperature.

(a) monitor 1000 λ = 1.001 A° (McMaster triple axis)

(hkℓ)	2θ	I	ΔI	(hkℓ)	2θ	I	ΔI
$1\bar{1}1$	16.47°	1256	± 40	$02\bar{2}$	27.06°	4744	± 90
$11\bar{1}$		1229	± 40	$2\bar{2}2$	33.3	2205	± 60
$\bar{1}1\bar{1}$		1387	± 50	$22\bar{2}$		1758	± 50
$\bar{1}\bar{1}1$		1375	± 50	$\bar{2}2\bar{2}$		2086	± 60
200	19.04	3839	± 80	$\bar{2}\bar{2}2$		2220	± 60
$\bar{2}00$		4125	± 90	400	38.64	2955	± 70
$0\bar{2}2$	27.06	5361	± 100	$\bar{4}00$		3514	± 80

(b) Averaged over symmetry related reflections and corrected for Lorentz factor.

(hkℓ)	$(\sin\theta/\lambda)^2$	$I_o = I\sin 2\theta$	Normalized to 200 point	$\ln I_o$
111	.02048	1488 ± 25	6966 ± 120	8.8488
200	.02732	5196 ± 80	24320 ± 370	10.0991
220	.05466	9194 ± 120	43033 ± 560	10.6697
222	.08197	4540 ± 60	21250 ± 280	9.9641
400	.1093	8080 ± 130	37819 ± 610	10.5406

Table IV-3: Data for least squares for Fig. IV-1.

Structure factor group	Slope ($A^{\circ 2}$)	Intercept	Relative intensities
(111)	- 1.344 ± .084	8.943 ± .014	7655 ± 110
(200)	- 1.884 ± .027	10.1438 ± .0057	25433 ± 150
(220)	- 1.967 ± .029	10.7716 ± .0058	47648 ± 270

each site are roughly equal or that the structure factor for each group is dominated by one of the scattering amplitude terms. The slopes of the least square fits as given in Table IV-3 for the (200) and (220) groups are very close to one another. This is to be expected since both of the structure factors are dominated by the relatively large $2b_{Ni}e^{-W_{Ni}}$ term. The magnitude of the slope of the (111) type group is 30% lower. Since b_{Ni} is not involved in this structure factor, the roles of the Debye-Waller factors for Mn, V and Sn become more important. This increases the likelihood of a different slope.

To obtain the relative peak intensities, proportional to $|F(\bar{Q})|^2$, the three lines are extrapolated to $(\sin\theta/\lambda)^2 = 0$. The intercepts are given in Table IV-3 along with the corresponding peak intensities. This data can now be compared with the model of an ordered crystal as discussed in the theory and shown in Table II-1. For easy comparison, the observed peak intensities are divided by the predicted structure factors squared and given below. Only relative intensities are meaningful.

(111) 7655/1.32 = 5800 ± 200

(200) 25433/4.89 = 5200 ± 140

(220) 47648/9.00 = 5300 ± 120

These ratios would be the same if the model was correct. The intensity for the (111) reflections is 5% too high.

If the statistical errors shown are assumed to be the only errors in these numbers, then the data must be explained by disorder. As the (111) intensity is probably high rather than the (200) and (220) being

low, a disorder effect must be found which increases the magnitude of this structure factor. Ni-Sn disorder would effect the relative intensities this way. For example, if 5% of the Sn-atoms on the Sn site were exchanged with Ni atoms on the Ni site, the above ratios would be

(111)	5547 ± 180
(200)	5457 ± 150
(220)	5300 ± 120

Since these numbers are equal within their statistical errors, the data is consistent with this model.

Because the points deviate from the straight line in the (111) group, the errors in the points were underestimated. Examination of the data in Table IV-1(a) shows that the intensities measured for symmetry related reflections also did not agree within these statistical errors. For instance, there is over 8% difference in intensity between the $(1\bar{1}1)$ and $(11\bar{1})$ reflections. In some cases, the discrepancy is greater. These discrepancies are due to something other than counting statistics. There are two possibilities. The first is crystal alignment. It should have been done to an accuracy better than 1°. An attempt was made in later experiments to increase this accuracy. Secondly, crystal shape dependent effects like those due to extinction and absorption were in play. It was hoped that averaging over symmetry related peaks would give accurate intensity ratios. However, if the apparent error was not random, then the differences might not average to zero. For this reason the value of 5% Ni-Sn disorder is not very certain.

The data for the experiments on crystal #3 is contained in Tables IV-4, 5 and 6 and in Fig. IV-2. The sample was mounted in the dewar and aligned at McMaster University for the work to be done at Chalk River.

Alignment was achieved to within 0.1° by masking off the crystal with cadmium so that the diffracted beam was only 2 mm in diameter. It was easy to pinpoint the direction of this outgoing beam by masking the counter. A very sensitive way to measure the angle of the beam with respect to the horizontal was the result. Simultaneous leveling of the beams reflected off the front and back of planes for two dissimilar reflections fixes the crystal's orientation. It was observed that the alignment changed by as much as 0.5° when the crystal and mounting mechanism was cooled to liquid nitrogen temperature. The alignment was repeated at the lower temperature and it was found to be reproducible when the crystal was cycled to room and back to low temperature.

Room temperature scans were taken of the (111), (200) and (220) peaks at a monitor setting of 20,000 counts. The wavelength was 1.15 A°. These are also plotted in Fig. IV-1, normalized to the (200) reflection. It is noted that the (220) point for this crystal is low, again due to extinction. Crystal #3 is somewhat thicker than crystal #2.

With liquid nitrogen in the inner dewar, the temperature of the sample was 78 K. The first magnetic data was taken under these conditions with a monitor setting of 40,000. The data is shown in Table IV-5 (a). There are a few problems with this run. The large amount of liquid nitrogen surrounding the small crystal reduced the intensity

Table IV-4: Bragg peak intensities for crystal #3 at room temperature

(a) monitor 20,000 λ = 1.15 A° (Chalk River triple axis)

(hkℓ)	2θ	I	ΔI
$1\bar{1}1$	18.9°	41790	± 260
$11\bar{1}$		36899	± 230
$\bar{1}1\bar{1}$		38426	± 240
$\bar{1}\bar{1}1$		39853	± 250
200	21.8°	105890	± 490
$\bar{2}00$		104256	± 490
$0\bar{2}2$	31.3°	118347	± 520
$02\bar{2}$		112790	± 510

(b) Averaged over symmetry related reflections and corrected for Lorentz factor.

(hkℓ)	$(\sin\theta/\lambda)^2$	$I_o = I\sin 2\theta$	Normalized	$\ln I_o$
111	.02048	50845 ± 160	7922	8.9775
200	.02732	156083 ± 510	24320	10.0091
220	.05466	240160 ± 760	37420	10.5300

Table IV-5: Bragg peak intensities for crystal #3 at T = 78 K.

(a) monitor 40,000 Liquid nitrogen in inner dewar λ = 1.15 A°

(hkℓ)	$I_{nucl} + \frac{2}{3} I_{mag}$	I_{nucl}	I_{mag}	I_{mag}/I_{nucl}
$1\bar{1}1$	50666 ± 320	40469 ± 300	15296 ± 440	.378 ± .02
$11\bar{1}$	51526 ± 320	40850 ± 290	16014 ± 430	.392 ± .02
$\bar{1}1\bar{1}$	46852 ± 300	34550 ± 270	18453 ± 400	.534 ± .02
$\bar{1}\bar{1}1$	55136 ± 340	42643 ± 290	18740 ± 450	.439 ± .02

(b) Averaged over symmetry related reflections and corrected for Lorentz factor.

(hkℓ)	I_{onucl}	I_{omag}	$(I_{mag}/I_{nucl})_{av}$
111	51345 ± 190	22189 ± 280	.436 ± .02

Table IV-6: Bragg peak intensities for crystal #3 at T = 117 K.

(a) monitor 20,000:' 40,000:" He_2 in inner dewar λ = 1.15 A°

(hkℓ)	$I_{nucl} + \frac{2}{3} I_{mag}$	I_{nucl}	I_{mag}	I_{mag}/I_{nucl}
$1\bar{1}1'$	51310 ± 290	41666 ± 270	14466 ± 590	.347 ± .02
$11\bar{1}'$	52373 ± 290	40831 ± 250	17313 ± 570	.424 ±
$\bar{1}1\bar{1}'$	51448 ± 290	37685 ± 240	20645 ± 570	.548 ±
$\bar{1}\bar{1}1'$	57033 ± 320	45577 ± 270	17184 ± 630	.377 ±
200'	116116 ± 520	107474 ± 490	12963 ± 1100	.121 ± .01
$\bar{2}00'$	121343 ± 550	112871 ± 520	12708 ± 1100	.113 ± .01
$0\bar{2}2"$	269655 ± 840	261407 ± 820	12372 ± 1800	.0473 ± .007
$02\bar{2}"$	248208 ± 780	239273 ± 770	13403 ± 1600	.0560 .007

(b) Averaged over symmetry related reflections and corrected for Lorentz factor.

(hkℓ)	I_{onucl}	I_{omag}	$(I_{mag}/I_{nucl})_{av}$
111	53692 ± 170	22547 ± 380	.424 ± .02
200	163658 ± 530	19067 ± 1200	.117 ± .02
220	260113 ± 580	13391 ± 1250	.0517 ± .007

Fig. IV-2: Typical Bragg peaks for crystal #3.

● magnet off

X magnet on

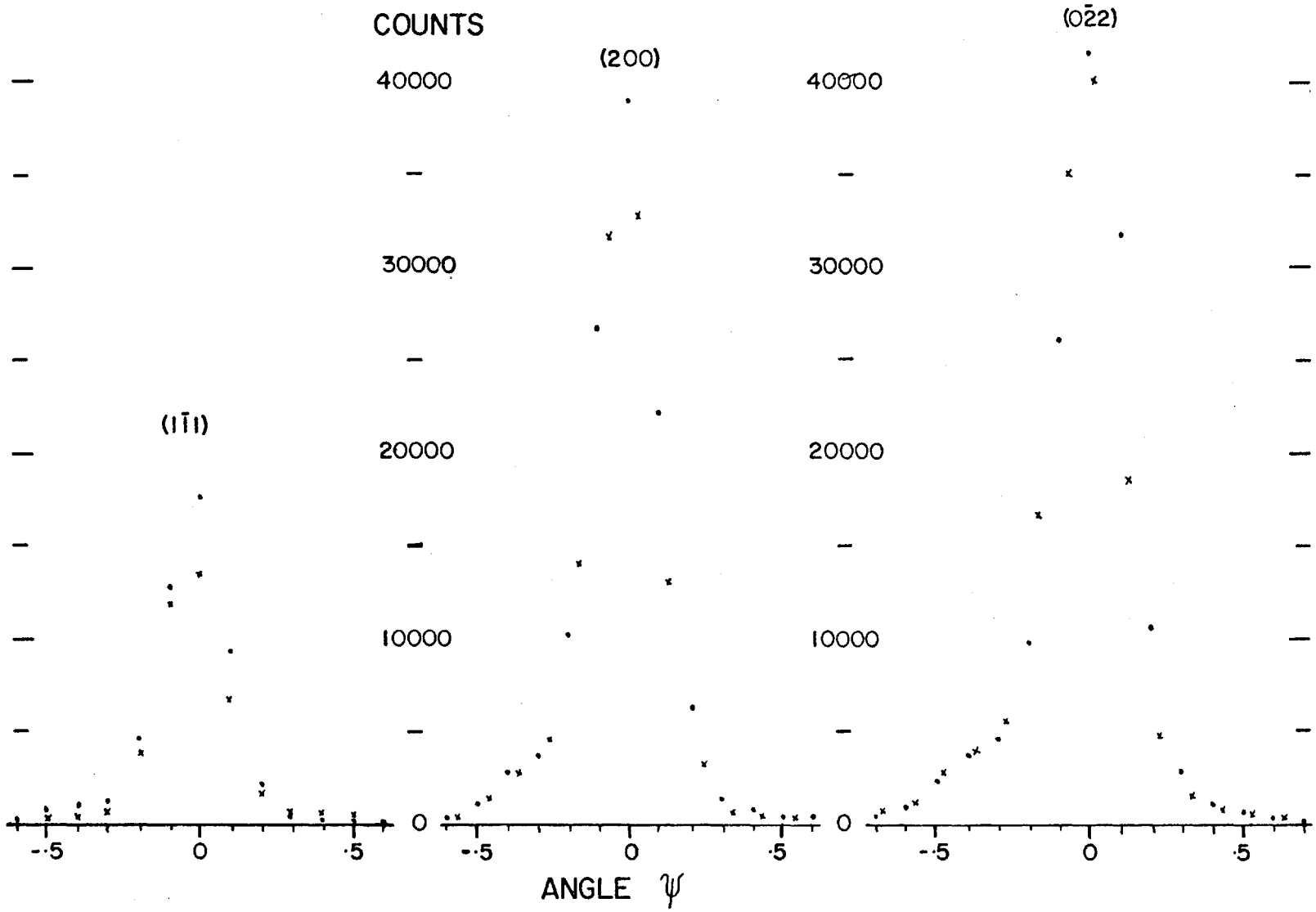
COUNTS
(200)
(0$\bar{2}$2)
(1$\bar{1}$1)
40000
30000
20000
10000
0
-·5
0
·5
ANGLE ψ

from the crystal and produced a large background. The (111) data was given for comparison but the weaker magnetic reflections were buried in the noise. It was found that replacing the nitrogen in the dewar with helium exchange gas increased the intensities by a factor of 2 and almost eliminated the background contribution.

The final set of data appears in Table IV-6 and Fig. IV-2. With the inner dewar compartment filled with helium, the temperature of the sample was 117 K. The monitor was set at 20,000.

The nuclear scattering intensities and magnetic scattering intensities were determined from the combined scattering by controlling the magnetic scattering with a saturating magnetic field. When the sample was magnetized along the scattering vector, no magnetic scattering took place. When there was no magnetic field present, two thirds of the magnetic scattering occured along with the nuclear scattering. The integrated intensities obtained by this magnet on-magnet off method are given in the table along with the ratio of magnetic to nuclear intensities. Some representative data is plotted in Fig. IV-2.

Since we already have obtained an idea of the chemical order from the room temperature part of the experiment, the information on magnetic moment distribution can be obtained from the ratios mentioned above. For any particular peak, the ratio should be independent of crystal shape effects.

To compare the data with theory, we need only compare these ratios with those calculated from the model. The ratios for the (111) reflections do not agree within the statistical error. For this reason,

the error quoted below is the standard error of the mean. The tolerances in the theoretical ratios are due to the uncertainty in the scattering lengths.

hkℓ	Theory	Experiment
111	.569 ± .018	.424 ± .04
200	.134 ± .005	.117 ± .02
220	.041 ± .002	.052 ± .007

The ratios for the (220) reflection are nearly equal within the estimated error. We know from our bulk magnetization analysis that there must be, on average, 3.2 μ_B of moment per unit cell. It is the nature of the structure factor for this reflection that the nuclear intensity is independent of chemical disorder and the magnetic intensity is independent of which atoms have the magnetic moments and where the atoms are located. These ratios therefore have to agree within experimental error, barring extinction. Due to the statistical nature of the standard error, there is a 30% chance that the ratios agree. At any rate, the error is presumed to be slightly underestimated. The agreement is good, keeping in mind the scatter in the (111) data and that, due to the form factor, the magnetic scattering is only 5% of the total. The ratios for the (200) are equal within experimental error but the ratio obtained for the (111) reflection is low compared to the model. To explain this in terms of magnetic disorder, assuming that the crystal is chemically ordered, moment must be taken off the Y site (Mn and V) atoms and given to the Z site (Sn) atoms. To calculate

what the moment distribution is, let a fraction ν of the 3.2 μ_B be situated on the Y site. The following relation,

$$\frac{F_M(\text{disordered})}{F_M(\text{ordered})} \propto \frac{|\nu - (1-\nu)|^2}{1} = |2\nu-1|^2 = \frac{.424 \pm .04}{.569 \pm .018} = .75 \pm .09,$$

gives the value $\nu = .933 \pm .026$. The predicted moment on the Y-site is therefore $2.99 \pm .08$ μ_B and on the Z site is $.21 \pm .08$ μ_B. If all the Y site moment existed on the Mn atoms and none on the V atoms, the moments would be $3.74 \pm .10$ μ_B per Mn atom and $.21 \pm .08$ μ_B per Sn atom.

These are unanticipated results. The moment on the Mn atom is expected to be 4 μ_B and on all the other atoms, zero. It is difficult to explain the drop in the (111) magnetic intensity in terms of disorder. Other structures where the Mn atoms are closer together are antiferromagnetic so any non Y-site moments in the Heusler alloy structure should point in the opposite direction. Chemical or magnetic disorder which incorporates this effect does not decrease the (111) ratio.

There is some evidence (Felcher, 1963) that in a Heusler alloy, a small moment may exist on the X-site atoms. There is no evidence for a moment on the Sn atoms. The Z-site moment could be explained by Mn - Sn disorder but this did not show up in the nuclear scattering results. The value of $3.74 \pm .10$ μ_B per Mn atom is smaller than the 4.05 μ_B obtained for Ni_2MnSn by Webster (1969). The value 3.74 μ_B is obtained from the (111) data in Table IV-6.

As discussed above, the (111) data appears to have a systematic error. It was stated above that the ratios quoted should be independent

of crystal shape effects. The disagreement between the symmetry related peaks, however, is quite large. It is suspected that either the "saturating" magnetic field was not large enough or the crystal mount was bending in the magnetic field. The intensity of the $(11\bar{1})$ peak is plotted as a fn-of current through the magnet in Fig. IV-3. Evidently the intensity did not level off with increased magnetic field. This example is probably the worst case. These effects are impossible to correct analytically and elimination requires a changed design and repeating the measurements.

The (111) ratios were calculated by an alternate method where the nuclear intensities were obtained from the room temperature data instead of the magnet-on case. Corrections for the Debye-Waller factor were estimated from the other room temperature data. The result of this calculation is a moment of $3.82 \pm .10\ \mu_B$ per Mn atom.

Fig. IV-3: Field dependence of $(11\bar{1})$ intensity.

T = 117 K

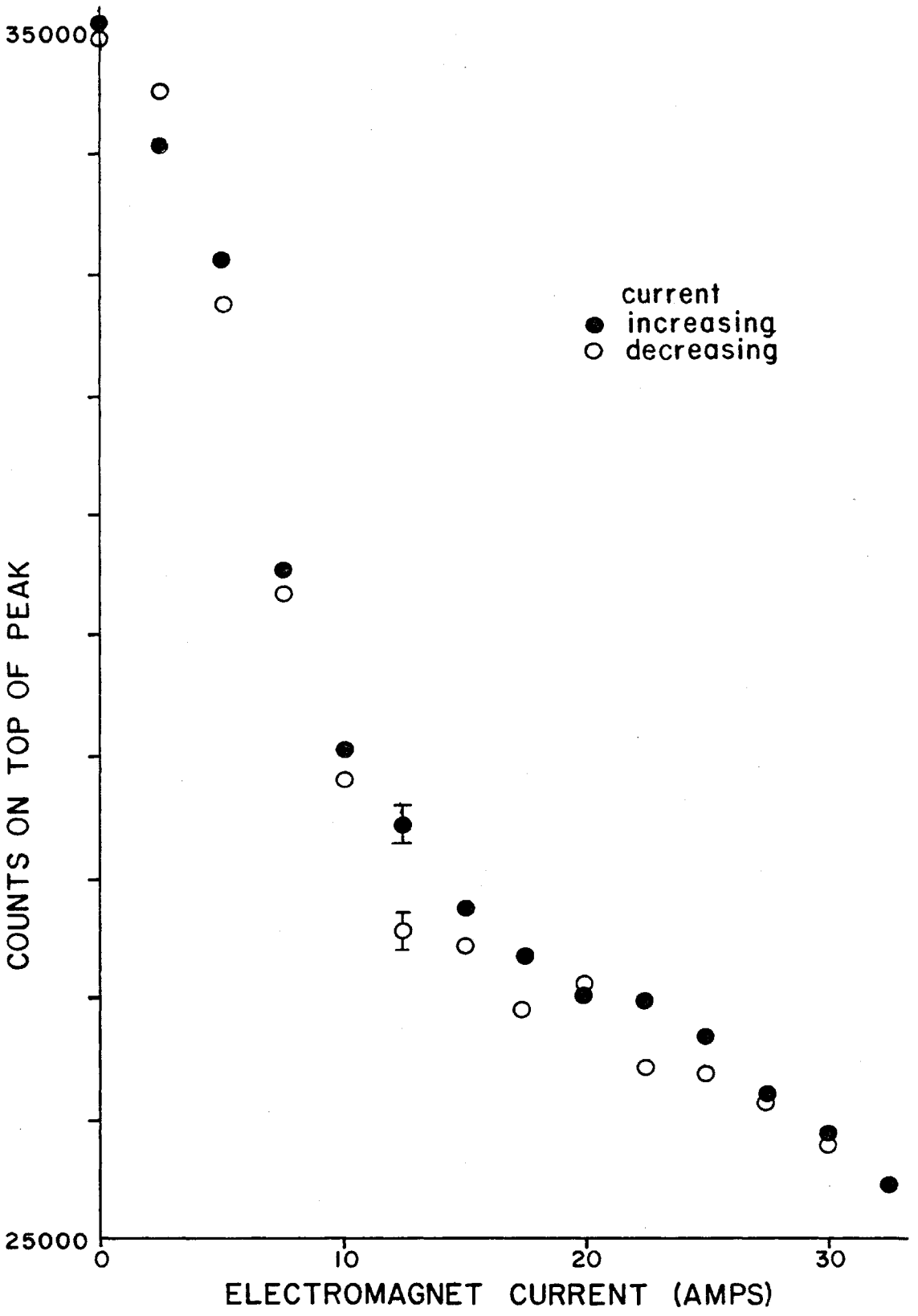
35000
25000
0
10
20
30
COUNTS ON TOP OF PEAK
ELECTROMAGNET CURRENT (AMPS)
current
increasing
decreasing

CHAPTER V

CONCLUSIONS

The chemical and magnetic disorder in a single crystal of $Ni_2Mn_{0.8}V_{0.2}Sn$ have been measured by neutron diffraction. This crystal has the Heusler $L2_1$ structure with the Mn and V atoms randomly distributed on one of the four FCC sublattices.

A large single crystal of $Ni_2Mn_{0.8}V_{0.2}Sn$ was grown by the Czochrolski method. It is important that the melt material be free of oxide to prevent small crystals from occuring in the boule. The material is easily cut by spark erosion. The mozaic spread of the crystal was less than 30'.

Nuclear Bragg peak intensities were measured for diffraction planes parallel to the (110) direction, up to a value of $(\frac{\sin\theta}{\lambda})^2 = .3279$. The intensities in each of the three structure factor groups decrease exponentially with increasing $(\frac{\sin\theta}{\lambda})^2$. This was due to phonon scattering. The resulting Debye-Waller factors were measured to be:

$$2W(111) = (1.344 \pm .084\ A^{\circ 2}) \times (\frac{\sin\theta}{\lambda})^2$$

$$2W(200) = (1.884 \pm .027\ A^{\circ 2}) \times (\frac{\sin\theta}{\lambda})^2$$

$$2W(220) = (1.967 \pm .029\ A^{\circ 2}) \times (\frac{\sin\theta}{\lambda})^2$$

The curves for each group of reflections were extropolated to $\frac{\sin\theta}{\lambda} = 0$ to obtain the intensity ratios. It is necessary to incorporate

(5 ± 4)% Ni-Sn disorder into the model to obtain agreement between the measured nuclear Bragg peak intensity ratios and the calculated structure factor ratios. The large uncertainty in this number is due to problems with alignment and extinction and is apparent because the symmetry related intensities do not agree. It is possible that 5% of the Sn atoms are interchanged with Ni atoms but the results are inconclusive.

To sufficiently reduce the effects of extinction, long thin crystals less than 1 mm thick must be used.

The magnetic Bragg peak intensities were measured by the non-polarized neutron method of controlling the magnitude of the magnetic interaction vector $\bar{q}$. These intensity ratios are compared with the structure factor ratios calculated from a model of the magnetic structure. Bulk magnetization measurements on $Ni_2Mn_{0.8}V_{0.2}Sn$ give a value of 262 ± 3 K for the Curie temperature and 3.19 ± 0.3 μ_B/mol. This result is in good agreement with the expected 0.8 Mn atoms/mol and 4 μ_B/Mn atom. Using this result, and the measured intensity ratios, the magnetic moment distribution for the crystal is 2.99 ± .08 μ_B/Mn site and .21 ± .08 μ_B/Sn site. If the crystal is chemically ordered and all Mn-site moment exists on the Mn atoms and none on the V atoms then the magnetic moment per Mn atom is 3.74 ± .10 μ_B. This value is low in comparison to the 4 μ_B/Mn atom usually obtained for Heusler alloys.

If the experiments were repeated, a crystal holder should be designed that removes any suspicion of crystal motion when the magnetic field is applied. It was possible that the magnetic field was not large enough but this is unlikely.

BIBLIOGRAPHY

BACON, G.E., Neutron Diffraction, 3rd ed., Oxford [Eng.]: Clarendon Press, 1975.

BRADLEY, A.J. and RODGERS, J.W., Proc. R. Soc. Lond. A144, 340 (1934).

CAMPBELL, C.C.M., J. Phys. F(Met. Phys.), Oct. 1975, 5 (10) 1931-1945.

CAMPBELL, C.C.M. and STAGER, C.V., Can. J. Phys., 1976, 54 (21) 2197-2203.

CASTELLIZ, L., M. Chem. 84, 765 (1953).

CASTELLIZ, L., M. Chem. 82, 1059 (1951).

FELCHER, J.P., CABLE, J.W. and WILKINSON, M.K., J. Phys. Chem. Solids 24, 1663 (1963).

FONER, S., Rev. Sci. Instr. 30, 548 (1959).

HALLMAN, E.D., The Crystal Dynamics of Face Centered Cubic Iron Group Alloys. Thesis, McMaster University (1969).

HAMES, F.A., J. Appl. Phys. 31, 370S (1960).

HAMILTON, W.C., Acta. Cryst. 10, 629 (1957).

HEUSLER, F., STARCK, W. and HAUPT, E., Verh. der deut. phys. Gesell., 5, 220 (1903).

ISHIKAWA, Y., TAJIMA, K. and RADHAKRISHNA, P., J. Phys. Soc. Japan, 40 (6) 1597 (1976).

JOHNSTON, G.B. and HALL, E.O., J. Phys. Chem. Solids 29, 193 (1968).

MARSHALL, W. and LOVESEY, S.W., Theory of Thermal Neutron Scattering, Oxford U.P., Oxford, England, 1971.

NODA, Y. and ISHIKAWA, Y., J. Phys. Soc. Japan, 40, 699 (1976).

NODA, Y. and ISHIKAWA, Y., J. Phys. Soc. Japan, 40, 690 (1976).

ROWE, J.M., Neutron Spectroscopy: The Design and Construction of a Triple Axis Crystal Spectrometer, and a study of the Lattice Dynamics of Metals. Thesis, McMaster University (1966).

WEBSTER, P.J., The Magnetic and Chemical Structures of the Heusler Alloys. Thesis, Sheffield University (1968).

WEBSTER, P.J., Contemp. Phys. 10, 559 (1969).

ZACHARISON, W.H., Acta. Cryst. 16, 1139 (1963).